A Combined Reduced Order-Full Order Methodology for the Solution of 3D Magneto-Mechanical Problems with Application to MRI Scanners

M. Seoane*,†,‡, P.D. Ledger†, A.J. Gil†, S. Zlotnik‡ and M. Mallett*

* Siemens Healthineers, MR Magnet Technology, Wharf Road, Eynsham, Witney, OX29 4BP, United Kingdom

†Zienkiewicz Centre for Computational Engineering, College of Engineering, Swansea University, Bay Campus, Swansea, SA1 8EN, United Kingdom

‡Laboratori de Càlcul Numèric, Universitat Politècnica de Catalunya, c/ Jordi Girona 1-3 Edifici C2, 08034, Barcelona, Spain

March 17, 2020

Abstract

The design of a new MRI scanner requires multiple numerical simulations of the same magneto-mechanical problem for varying model parameters, such as frequency and electric conductivity, in order to ensure that the vibrations, noise and heat dissipation are minimized. The high computational cost required for these repeated simulations leads to a bottleneck in the design process due to an increased design time and, thus, a higher cost. To alleviate these issues, the application of reduced order modelling techniques, which are able to find a general solution to high dimensional parametric problems in a very efficient manner, is considered. Building on the established Proper Orthogonal Decomposition (POD) technique available in the literature, the main novelty of this work is an efficient implementation for the solution of 3D magneto-mechanical problems in the context of challenging MRI configurations. This methodology provides a general solution for varying parameters of interest. The accuracy and efficiency of the method is proven by applying it to challenging MRI configurations and comparing with the full order solution.
Keywords: ROM, Proper Orthogonal Decomposition, Magneto-mechanical coupling, MRI scanner, Multifield systems, Newton methods, Lagrangian.

1 Introduction

Magnetic Resonance Imaging (MRI) scanners have become an essential tool in the medical industry due to their ability to produce high quality images of the human body. MRI scanners have been proven to be especially efficient in the diagnosis of vascular problems, tumours or internal bleeding, among others. Superconducting MRI scanners, Figure 1, are the most common type used for diagnostic imaging and they essentially consist of three main components: cryostat, main coils and gradient coils. The cryostat is formed by several radiation shields (typically 4K, 77K and Outer Vacuum Chamber (OVC) shields) that prevent radiation from heating the liquid helium that is used to keep the superconducting main coils at a temperature of 4K. The main coils generate a strong static magnetic field while the gradient coils generate time varying pulsed magnetic fields. These fields excite the protons in the human body generating a signal that is used to construct an image of the body.

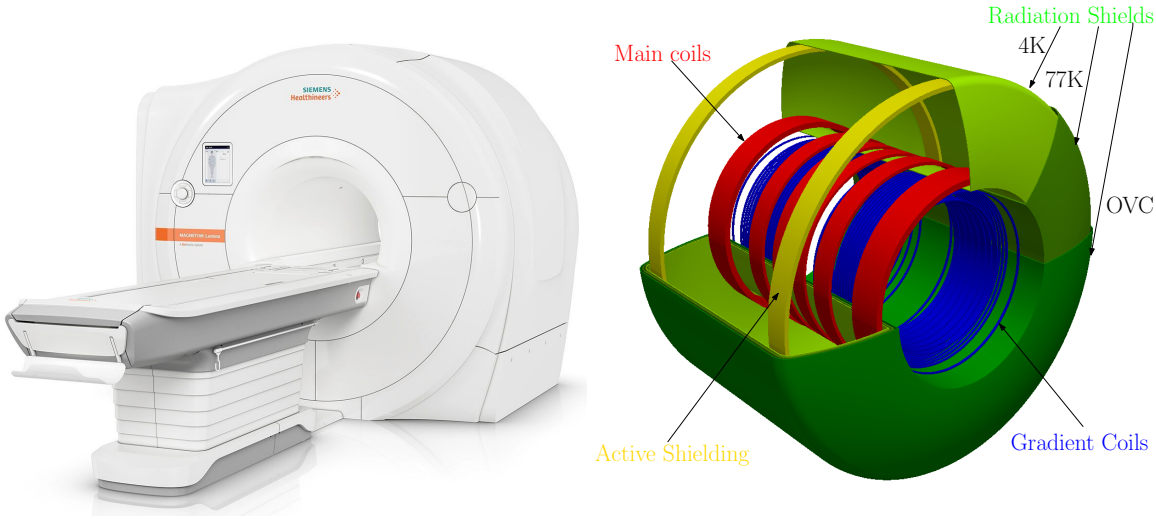

(a) Magnetom Lumina

(b) MRI main components

Figure 1: MRI scanner. (a) New model Magnetom Lumina 3T. Image Courtesy of Siemens Healthineers. (b) Illustration of the main components: main coils, gradient coils and radiation shields (4K, 77K and Outer Vacuum Chamber (OVC)).

The transient magnetic field generated by the gradient coils induces eddy currents in the conducting radiation shields, which leads to vibrations and the dissipation of heat [22, 4, 39]. These vibrations cause a reduction in image quality, while the dissipation of heat can cause helium boil-off and potentially result in a magnet quench[1]. To minimise these effects, a coupled physics magneto-mechanical problem must be solved repeatedly for different model parameters, including frequency and electric conductivity among others, in order to find the optimal combination of parameters for the desired performance. Multiple attempts at modelling these effects have been made, including the application of finite difference time domain methods for the prediction of induced eddy currents but neglecting mechanical effects [14, 42, 26], or low order temporal finite element schemes for the solution of the coupled magneto-mechanical problem [35]. In previous work by our research group, a hp-finite element formulation for the solution of the magneto-mechanical problem of interest in axisymmetric configurations was proposed [22, 4, 3]. This was based on a linearised approach using an AC-DC splitting and assuming small displacements and velocities. This work was then extended in [39] to consider the general three-dimensional (3D) case and assuming small displacements but not necessarily small velocities. In [39] a new Lagrangian formulation was used, which results in an efficient staggered scheme.

Although the formulation developed in [39] results in an accurate and efficient solver, a bottleneck still arises in the design process of a new MRI configuration due to the need to solve the problem repeatedly for varying frequencies and material properties. These variations affect the system to be solved and therefore cannot be tackled with a simple factorization. The high computational cost required by these multiple simulations results in an increase of the total time required to obtain a new MRI design, which has financial implications. In order to optimise this process, Reduced Order Models (ROMs) are considered here. ROMs allow to describe a family of solutions (usually arising from parametric partial differential equations) in terms of a reduced basis. The term "reduced" is used here to denote a basis whose size is much smaller than a standard Finite Element (FE) basis. The later is denoted in this context as "full order" or "high fidelity" model [10, 1, 16, 8]. The reduction of the size of the basis in which the solution is sought has an immediate impact in the size of the matrix to be inverted and, therefore, in the computational cost of the method.

Several numerical techniques can be classified as ROMs. Some examples are Proper Generalised Decomposition (PGD) [10, 28, 11] and Proper Orthogonal Decomposition (POD) [8, 25, 44, 9], whose variants

[1] A quench refers to the sudden loss of superconductivity when its temperature is raised.

include POD with interpolation (PODI) [34, 33, 7] and projection based POD (in the following PODP), also known as POD based Reduced Basis (RB) or POD-Galerkin [40, 13, 12]. One key difference between PGD and POD is the complexity of their implementation and the extent to which an existing FE solver must be modified to implement the corresponding ROM. This is usually called the intrusiveness of the technique; a non-intrusive technique can be used "on top" of an existing FE solver without any modification. PGD is typically much more intrusive than POD. The intrusiveness, despite being independent of the numerical effectiveness of the technique, is sometimes crucial in the context of industrial applications, when some software might already have been certified for a particular application. Hence, in this work, the application of POD to the coupled magneto-mechanical MRI problem previously discussed is considered. In particular, the discrete POD version, which is also referred to as Principal Component Analysis (PCA) in the literature [8, 29], will be used in this work.

In the context of numerical simulations in engineering, POD has successfully been applied to different areas including mechanics [29, 32], thermal problems [44, 5], fluid flow [27, 31] as well as electromagnetic problems with application to integrated circuits [19]. In such problems, POD involves two stages in the solution of the parametric problem. During the first stage, the basis to represent the solution is chosen. To build this basis, many FE solutions need to be obtained and, therefore, this stage is computationally expensive, although this can be mitigated as it is trivially parallelizable and needs only to be done once. From the computed solutions, we choose in this work to obtain the basis via a Singular Value Decomposition (SVD) [6, 15]. The second stage, performed once the basis has been chosen, involves finding the solution for a given set of parameters. In the case of PODI, this second phase consists simply in interpolating the parametric modes (right singular vectors), while in the case of PODP, it involves the solution of a reduced linear system of equations with the same size as the chosen basis. Given that this size is reduced, this second stage is significantly computationally cheaper than the first stage to the extent that the solution can be obtained in real time. This two stage scheme becomes efficient when the second stage is applied many times (multiple queries) or when the second stage has to be solved very fast (fast queries).

Building on the established POD technique [8, 9], the main novelty of this work is an efficient implementation for the solution of 3D magneto-mechanical problems in the context of MRI scanners. Our implementation exploits the staggered nature of the linearised Lagrangian approach developed in [39] by building a ROM to approximate the electromagnetic solution and using this to feed the mechanical full order solver. First, the application of POD to the complete problem is studied and we show that the number of samples required to obtain an accurate approximation is very large and, thus, no computational speed-up can be obtained. Then, the combined reduced order-full order methodology is presented and we show its accuracy and efficiency by applying it to challenging MRI configurations. Furthermore, a comparison between PODI and PODP is performed, which shows the additional benefits offered by the latter.

The structure of the article is as follows; Section 2 presents the full order model, including boundary and transmission conditions. The AC-DC splitting used to linearise the problem and our formulation in the frequency domain are briefly described in Section 3. The discrete system, which is the starting point for the construction of our ROM, is then stated in Section 4. The application of a ROM to the magneto-mechanical problem of interest is discussed in Section 5, where a complete description of the POD is first presented in Section 5.1 followed by the combined reduced order-full order methodology in Section 5.3. A series of numerical results are presented in Section 6, where the accuracy and efficiency of these methodologies is assessed by applying them to challenging MRI configurations. The document finishes with concluding remarks in Section 7.

2 Problem Statement

In this section, the magneto-mechanical problem of interest in a Lagrangian frame is stated [39]. Consider a magneto-mechanical problem set on a truncated unbounded domain $\Omega = \Omega_C \cup \Omega_{NC}$, where $\Omega_C = \bigcup_{n=1}^{N_C} \Omega_{C,n}$ denotes the union of N_C disjoint elastic conducting bodies, with electric conductivity $\gamma \neq 0$ and magnetic permeability μ possibly different from the vacuum permeability, $\mu_0 = 4\pi \times 10^{-7}$, and

$\Omega_{NC} := \Omega \backslash \overline{\Omega_C}$ [2] denotes the non-conducting region (Figure 2). Defining $\boldsymbol{E}_0$, $\boldsymbol{H}_0$ and $\boldsymbol{B}_0$ as the electric field intensity, magnetic field intensity and magnetic flux density in the Lagrangian frame, respectively, and introducing a magnetic vector potential $\boldsymbol{A}$ such that $\boldsymbol{B}_0 = \operatorname{curl} \boldsymbol{A}$ the problem can be formulated in terms of the magnetic vector potential and mechanical displacements, $\boldsymbol{u}$, as [39]: Find $(\boldsymbol{A}, \boldsymbol{u})(t) \in (\mathbb{R}^3 \times \mathbb{R}^3)(0, T]$ such that

$$\operatorname{curl}(\mu^{-1} \operatorname{curl} \boldsymbol{A}) + \gamma \frac{\partial \boldsymbol{A}}{\partial t} = \boldsymbol{0} \qquad \text{in } \Omega_C, \tag{1a}$$

$$\operatorname{curl}(\mu_0^{-1} \operatorname{curl} \boldsymbol{A}) = \boldsymbol{J}_0 \qquad \text{in } \Omega_{NC}, \tag{1b}$$

$$\operatorname{div} \boldsymbol{A} = 0 \qquad \text{in } \Omega_{NC}, \tag{1c}$$

$$\operatorname{div}(\boldsymbol{\sigma}^m(\boldsymbol{u}) + \boldsymbol{\sigma}^e(\boldsymbol{A})) = \rho \frac{\partial^2 \boldsymbol{u}}{\partial t^2} \qquad \text{in } \Omega_C, \tag{1d}$$

$$\boldsymbol{\sigma}^e(\boldsymbol{A}) := \mu^{-1} \left(\operatorname{curl} \boldsymbol{A} \otimes \operatorname{curl} \boldsymbol{A} - \frac{1}{2} |\operatorname{curl} \boldsymbol{A}|^2 \boldsymbol{I} \right) \qquad \text{in } \Omega_C, \tag{1e}$$

$$\boldsymbol{\sigma}^m(\boldsymbol{u}) := \boldsymbol{C} : \boldsymbol{\epsilon}(\boldsymbol{u}) \qquad \text{in } \Omega_C, \tag{1f}$$

$$\boldsymbol{n} \times \boldsymbol{A} = \boldsymbol{0} \qquad \text{on } \partial\Omega, \tag{1g}$$

$$\boldsymbol{u} = \boldsymbol{0} \qquad \text{on } \partial\Omega_C^D, \tag{1h}$$

$$[\boldsymbol{n} \times \boldsymbol{A}]_{\partial\Omega_C} = \boldsymbol{0} \qquad \text{on } \partial\Omega_C, \tag{1i}$$

$$[\boldsymbol{n} \times \mu^{-1} \operatorname{curl} \boldsymbol{A}]_{\partial\Omega_C} = \boldsymbol{0} \qquad \text{on } \partial\Omega_C, \tag{1j}$$

$$(\boldsymbol{\sigma}^e(\boldsymbol{A}) + \boldsymbol{\sigma}^m(\boldsymbol{u}))|^-_{\partial\Omega_C} \boldsymbol{n} = (\boldsymbol{\sigma}^e(\boldsymbol{A}))|^+_{\partial\Omega_C} \boldsymbol{n} \qquad \text{on } \partial\Omega_C^N, \tag{1k}$$

$$\boldsymbol{A}(t = 0) = \boldsymbol{0} \qquad \text{in } \Omega, \tag{1l}$$

$$\boldsymbol{u}(t = 0) = \frac{\partial \boldsymbol{u}}{\partial t}(t = 0) = \boldsymbol{0} \qquad \text{in } \Omega_C, \tag{1m}$$

where $\boldsymbol{J}_0$ is the solenoidal current source, ρ the material density, $\boldsymbol{n}$ a unit outward normal vector to $\partial\Omega_C$, $\boldsymbol{I}$ the rank 2 identity tensor, $[\boldsymbol{b}]_{\partial\Omega_C} = \boldsymbol{b}|^+ - \boldsymbol{b}|^-$ denotes the jump of $\boldsymbol{b}$ at $\partial\Omega_C := \overline{\partial\Omega_C^D} \cup \overline{\partial\Omega_C^N}$ and $\boldsymbol{b}|^+$, $\boldsymbol{b}|^-$ denote the evaluation of $\boldsymbol{b}$ at the outside and inside of $\partial\Omega_C$, respectively. Furthermore, we have chosen to set the initial conditions for the fields to be zero, corresponding to a system at rest at $t = 0$. In the above, the far field decay of $\boldsymbol{A} = O\left(|\boldsymbol{x}|^{-1}\right)$ as $|\boldsymbol{x}| \to \infty$ (where $\boldsymbol{x} = (x_1, x_2, x_3) = (x, y, z)$ is the position vector) in an unbounded domain has been approximated by the condition $\boldsymbol{n} \times \boldsymbol{A} = \boldsymbol{0}$ on $\partial\Omega$, which we assumed to be placed sufficiently far from Ω_C. Furthermore, the Maxwell and Cauchy stress tensors are denoted by $\boldsymbol{\sigma}^e$ and $\boldsymbol{\sigma}^m$, respectively, $\boldsymbol{\epsilon}(\boldsymbol{u}) := ((\nabla \boldsymbol{u} + (\nabla \boldsymbol{u})^T)/2$ is the small strain tensor and $\boldsymbol{C} = \boldsymbol{C}_{ijk\ell} \boldsymbol{e}_i \otimes \boldsymbol{e}_j \otimes \boldsymbol{e}_k \otimes \boldsymbol{e}_\ell$ is a rank 4 constitutive tensor with entries

$$\boldsymbol{C}_{ijkl} := \lambda \delta_{ij} \delta_{kl} + G \left(\delta_{ik} \delta_{jl} + \delta_{il} \delta_{jk} \right), \tag{2}$$

with δ_{ij} the Kronecker delta, $\boldsymbol{e}_i$ the ith unit basis vector and λ and G the Lamé parameters.
The physical (Eulerian) electric and magnetic fields are coupled to $\boldsymbol{A}$ and $\boldsymbol{v} = \frac{\partial \boldsymbol{u}}{\partial t}$ through

$$\boldsymbol{E} = -\frac{\partial \boldsymbol{A}}{\partial t} + \boldsymbol{B}_0 \times \boldsymbol{v} \qquad \text{in } \Omega_C, \tag{3a}$$

$$\boldsymbol{H} = \mu^{-1} \boldsymbol{B}_0 = \mu^{-1} \operatorname{curl} \boldsymbol{A} \qquad \text{in } \Omega, \tag{3b}$$

which can be applied once (1) is solved.

3 AC-DC Splitting and Weak Formulation

Following the methodology first presented in [4], an AC-DC splitting of the fields is introduced where the DC fields are induced by the current source $\boldsymbol{J}^{DC}$ of the main coils and the AC fields by the current source

[2] We will use an overbar to denote both completion of a domain to include its boundaries and the complex conjugate, however, it will always be clear which definition applies so no confusion should arise.

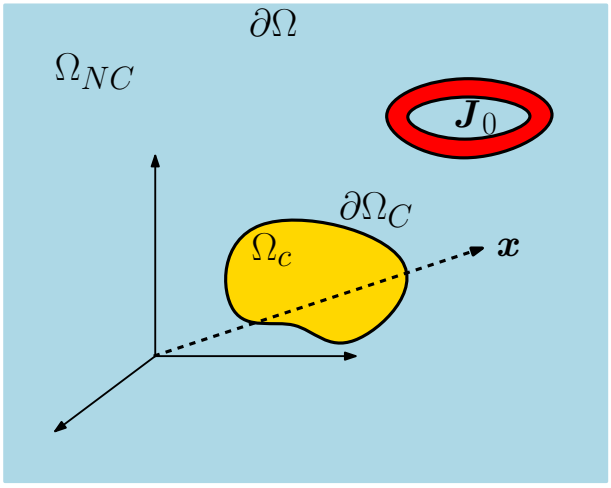

Figure 2: Magneto-mechanical coupled problem: General representation of the problem illustrating the different components involved.

$\boldsymbol{J}^{AC}$ of the gradient coils. The AC problem can then be linearised about the static solution $\boldsymbol{u}^{DC}$ and $\boldsymbol{A}^{DC}$, given that, in MRI applications, the DC magnetic field is much stronger than the AC field. This leads to an AC problem that is linear in the time dependent variables $\boldsymbol{u}^{AC}$ and $\boldsymbol{A}^{AC}$ and, thus, the problem can be formulated in the frequency domain by assuming a time-harmonic variation of the fields [4, 2, 39]. The total time dependent fields can then be expressed in terms of their DC and AC contributions as

$$\boldsymbol{A}(t) = \boldsymbol{A}^{DC} + \mathrm{Re}\left(\boldsymbol{\mathcal{A}}^{AC} e^{\mathrm{i}\omega t}\right), \tag{4a}$$

$$\boldsymbol{u}(t) = \boldsymbol{u}^{DC} + \mathrm{Re}\left(\boldsymbol{\mathcal{U}}^{AC} e^{\mathrm{i}\omega t}\right), \tag{4b}$$

$$\boldsymbol{J}_0(t) = \boldsymbol{J}^{DC} + \mathrm{Re}\left(\boldsymbol{\mathcal{J}}^{AC} e^{\mathrm{i}\omega t}\right), \tag{4c}$$

where $\omega = 2\pi f$ is the angular frequency, f is the frequency, and $\boldsymbol{\mathcal{A}}^{AC}$, $\boldsymbol{\mathcal{U}}^{AC}$ and $\boldsymbol{\mathcal{J}}^{AC}$ represent the complex amplitudes of the time varying AC fields $\boldsymbol{u}^{AC}$, $\boldsymbol{A}^{AC}$ and $\boldsymbol{J}^{AC}$ [3], respectively. For further details we refer to [39] where this methodology was applied to the three dimensional magneto-mechanical problem of interest. Below, we briefly summarise the weak variational statements that were obtained in this work.

3.1 Variational Formulation

In order to present the weak formulation of the problem, we define

$$\tilde{X}_\Omega := \{\boldsymbol{A} \in \boldsymbol{H}(\mathrm{curl}, \Omega) : \boldsymbol{n} \times \boldsymbol{A} = \boldsymbol{0} \text{ on } \partial\Omega\},$$

$$Y := \left\{\boldsymbol{u} \in \left(H^1(\Omega_C)\right)^3 : \boldsymbol{u} = \boldsymbol{0} \text{ on } \partial\Omega_C^D\right\}.$$

Let $\boldsymbol{w} = \left(w_1, w_2, \ldots, w_{N_p}\right)$ denote a general list of model parameters (frequency or conductivity of each shield among others). In this work we consider only parameters upon which the DC problem is independent, and thus we focus on the AC problem[4]. The variational formulation of the AC problem obtained in [39] can then be stated in the alternative form: Find complex solutions $\left(\boldsymbol{\mathcal{A}}_\varepsilon^{AC}, \boldsymbol{\mathcal{U}}^{AC}\right) \in \tilde{X}_\Omega \times Y$ such that

$$a_{\mathcal{A}_\varepsilon}\left(\boldsymbol{\mathcal{A}}_\varepsilon^{AC}(\boldsymbol{x}, \boldsymbol{w}), \delta\boldsymbol{A}(\boldsymbol{x}, \boldsymbol{w})\right) = r_{\mathcal{A}_\varepsilon}\left(\delta\boldsymbol{A}(\boldsymbol{x}, \boldsymbol{w})\right), \tag{5a}$$

$$a_{\mathcal{U}}\left(\boldsymbol{\mathcal{U}}^{AC}(\boldsymbol{x}, \boldsymbol{w}), \delta\boldsymbol{u}(\boldsymbol{x}, \boldsymbol{w}); \boldsymbol{A}_\varepsilon^{DC}(\boldsymbol{x}),\ \boldsymbol{\mathcal{A}}_\varepsilon^{AC}(\boldsymbol{x}, \boldsymbol{w})\right) = 0, \tag{5b}$$

[3] Note that a calligraphic font has been added to denote the complex amplitudes of the time-varying AC fields

[4] Note that the formulation is easily extendable to the case of parameters upon which the DC problem depends (e.g. permeability). However, in MRI applications the greatest interest typically lies in parameters that affect only the AC problem e.g. frequency or conductivity among others.

for all $(\delta\boldsymbol{A}, \delta\boldsymbol{u}) \in \tilde{X}_\Omega \times Y$, where

$$
\begin{aligned}
a_{\mathcal{A}_\varepsilon}\left(\boldsymbol{\mathcal{A}}_\varepsilon^{AC}(\boldsymbol{x},\boldsymbol{w}), \delta\boldsymbol{A}(\boldsymbol{x},\boldsymbol{w})\right) := & \int_\Omega \left(\mu^{-1}\operatorname{curl}\boldsymbol{\mathcal{A}}_\varepsilon^{AC}(\boldsymbol{x},\boldsymbol{w})\right)\cdot\left(\operatorname{curl}\overline{\delta\boldsymbol{A}(\boldsymbol{x},\boldsymbol{w})}\right)\,\mathrm{d}\Omega \\
& + \mathrm{i}\omega\int_{\Omega_C}\gamma\boldsymbol{\mathcal{A}}_\varepsilon^{AC}(\boldsymbol{x},\boldsymbol{w})\cdot\overline{\delta\boldsymbol{A}(\boldsymbol{x},\boldsymbol{w})}\,\mathrm{d}\Omega \\
& + \omega\varepsilon\int_{\Omega_{NC}}\boldsymbol{\mathcal{A}}_\varepsilon^{AC}(\boldsymbol{x},\boldsymbol{w})\cdot\overline{\delta\boldsymbol{A}(\boldsymbol{x},\boldsymbol{w})}\,\mathrm{d}\Omega, \qquad (6a)
\end{aligned}
$$

$$
\begin{aligned}
a_{\mathcal{U}}\left(\boldsymbol{\mathcal{U}}^{AC}(\boldsymbol{x},\boldsymbol{w}), \delta\boldsymbol{u}(\boldsymbol{x},\boldsymbol{w}); \boldsymbol{A}_\varepsilon^{DC}(\boldsymbol{x}),\ \boldsymbol{\mathcal{A}}_\varepsilon^{AC}(\boldsymbol{x},\boldsymbol{w})\right) := & \int_{\Omega_C}\boldsymbol{\sigma}^m(\boldsymbol{\mathcal{U}}^{AC}(\boldsymbol{x},\boldsymbol{w})) : \left(\operatorname{grad}\overline{\delta\boldsymbol{u}(\boldsymbol{x},\boldsymbol{w})}\right)\,\mathrm{d}\Omega \\
& - \omega^2\int_{\Omega_C}\rho\boldsymbol{\mathcal{U}}^{AC}(\boldsymbol{x},\boldsymbol{w})\cdot\overline{\delta\boldsymbol{u}(\boldsymbol{x},\boldsymbol{w})}\,\mathrm{d}\Omega \\
& + \int_{\Omega_C}\mu^{-1}S(\boldsymbol{A}_\varepsilon^{DC}(\boldsymbol{x}),\boldsymbol{\mathcal{A}}_\varepsilon^{AC}(\boldsymbol{x},\boldsymbol{w})) : \left(\operatorname{grad}\overline{\delta\boldsymbol{u}(\boldsymbol{x},\boldsymbol{w})}\right)\,\mathrm{d}\Omega \\
& - \int_{\partial\Omega_C^N}\mu^{-1}S(\boldsymbol{A}_\varepsilon^{DC}(\boldsymbol{x}),\boldsymbol{\mathcal{A}}_\varepsilon^{AC}(\boldsymbol{x},\boldsymbol{w}))\big|^+\,\boldsymbol{n}^-\cdot\overline{\delta\boldsymbol{u}(\boldsymbol{x},\boldsymbol{w})}\,\mathrm{ds}, \qquad (6b)
\end{aligned}
$$

$$
r_{\mathcal{A}_\varepsilon}\left(\delta\boldsymbol{A}(\boldsymbol{x},\boldsymbol{w})\right) := \int_{\mathrm{supp}(\boldsymbol{\jmath}^{AC})}\boldsymbol{\jmath}^{AC}(\boldsymbol{x})\cdot\overline{\delta\boldsymbol{A}(\boldsymbol{x},\boldsymbol{w})}\,\mathrm{d}\Omega, \qquad (6c)
$$

where

$$
\begin{aligned}
\mu^{-1}\boldsymbol{S}(\boldsymbol{A}^{DC},\boldsymbol{\mathcal{A}}^{AC}) := & \mu^{-1}\left(\operatorname{curl}\boldsymbol{A}^{DC}\otimes\operatorname{curl}\boldsymbol{\mathcal{A}}^{AC} + \operatorname{curl}\boldsymbol{\mathcal{A}}^{AC}\otimes\operatorname{curl}\boldsymbol{A}^{DC}\right. \\
& \left. -(\operatorname{curl}\boldsymbol{A}^{DC}\cdot\operatorname{curl}\boldsymbol{\mathcal{A}}^{AC})\boldsymbol{I}\right),
\end{aligned}
$$

is the linearised Maxwell stress tensor and regularisation has been applied to the problem as described in [39], being ε a small regularisation parameter.[5]. It should be remarked that in our previous work [39] the weights $\delta\boldsymbol{A}(\boldsymbol{x},\boldsymbol{w})$ and $\delta\boldsymbol{u}(\boldsymbol{x},\boldsymbol{w})$ were assumed to be real, which will no longer be the case in this article and, hence, these quantities appear with complex conjugates in (6). The expressions in (6) reduce to those in [39] when the weight is real. Note also that $a_{\mathcal{A}_\varepsilon}\left(\boldsymbol{\mathcal{A}}_\varepsilon^{AC}(\boldsymbol{x},\boldsymbol{w}), \delta\boldsymbol{A}(\boldsymbol{x},\boldsymbol{w})\right)$ is a sesquilinear form, $r_{\mathcal{A}_\varepsilon}\left(\delta\boldsymbol{A}(\boldsymbol{x},\boldsymbol{w})\right)$ is an antilinear form and $a_{\mathcal{U}}\left(\boldsymbol{\mathcal{U}}^{AC}(\boldsymbol{x},\boldsymbol{w}), \delta\boldsymbol{u}(\boldsymbol{x},\boldsymbol{w}); \boldsymbol{A}_\varepsilon^{DC}(\boldsymbol{x}),\boldsymbol{\mathcal{A}}_\varepsilon^{AC}(\boldsymbol{x},\boldsymbol{w})\right)$ can be rewritten as

$$
\begin{aligned}
a_{\mathcal{U}}\left(\boldsymbol{\mathcal{U}}^{AC}(\boldsymbol{x},\boldsymbol{w}), \delta\boldsymbol{u}(\boldsymbol{x},\boldsymbol{w}); \boldsymbol{A}_\varepsilon^{DC}(\boldsymbol{x}),\boldsymbol{\mathcal{A}}_\varepsilon^{AC}(\boldsymbol{x},\boldsymbol{w})\right) = & \tilde{a}_{\mathcal{U}}\left(\boldsymbol{\mathcal{U}}^{AC}(\boldsymbol{x},\boldsymbol{w}), \delta\boldsymbol{u}(\boldsymbol{x},\boldsymbol{w})\right) \\
& - \tilde{r}_{\mathcal{U}}\left(\delta\boldsymbol{u}(\boldsymbol{x},\boldsymbol{w}); \boldsymbol{A}_\varepsilon^{DC}(\boldsymbol{x}),\boldsymbol{\mathcal{A}}_\varepsilon^{AC}(\boldsymbol{x},\boldsymbol{w})\right), \qquad (7)
\end{aligned}
$$

where the sesquilinear $\tilde{a}_{\mathcal{U}}\left(\boldsymbol{\mathcal{U}}^{AC}(\boldsymbol{x},\boldsymbol{w}), \delta\boldsymbol{u}(\boldsymbol{x},\boldsymbol{w})\right)$ and antilinear $\tilde{r}_{\mathcal{U}}\left(\delta\boldsymbol{u}(\boldsymbol{x},\boldsymbol{w}); \boldsymbol{A}_\varepsilon^{DC}(\boldsymbol{x}),\boldsymbol{\mathcal{A}}_\varepsilon^{AC}(\boldsymbol{x},\boldsymbol{w})\right)$ forms are defined as

$$
\begin{aligned}
\tilde{a}_{\mathcal{U}}\left(\boldsymbol{\mathcal{U}}^{AC}(\boldsymbol{x},\boldsymbol{w}), \delta\boldsymbol{u}(\boldsymbol{x},\boldsymbol{w})\right) := & \int_{\Omega_C}\boldsymbol{\sigma}^m(\boldsymbol{\mathcal{U}}^{AC}(\boldsymbol{x},\boldsymbol{w})) : \left(\operatorname{grad}\overline{\delta\boldsymbol{u}(\boldsymbol{x},\boldsymbol{w})}\right)\,\mathrm{d}\Omega \\
& - \omega^2\int_{\Omega_C}\rho\boldsymbol{\mathcal{U}}^{AC}(\boldsymbol{x},\boldsymbol{w})\cdot\overline{\delta\boldsymbol{u}(\boldsymbol{x},\boldsymbol{w})}\,\mathrm{d}\Omega, \qquad (8a)
\end{aligned}
$$

$$
\begin{aligned}
\tilde{r}_{\mathcal{U}}\left(\delta\boldsymbol{u}(\boldsymbol{x},\boldsymbol{w}); \boldsymbol{A}_\varepsilon^{DC}(\boldsymbol{x}),\boldsymbol{\mathcal{A}}_\varepsilon^{AC}(\boldsymbol{x},\boldsymbol{w})\right) := & -\int_{\Omega_C}\mu^{-1}S(\boldsymbol{A}_\varepsilon^{DC}(\boldsymbol{x}),\boldsymbol{\mathcal{A}}_\varepsilon^{AC}(\boldsymbol{x},\boldsymbol{w})) : \left(\operatorname{grad}\overline{\delta\boldsymbol{u}(\boldsymbol{x},\boldsymbol{w})}\right)\,\mathrm{d}\Omega \\
& + \int_{\partial\Omega_C^N}\mu^{-1}S(\boldsymbol{A}_\varepsilon^{DC}(\boldsymbol{x}),\boldsymbol{\mathcal{A}}_\varepsilon^{AC}(\boldsymbol{x},\boldsymbol{w}))\big|^+\,\boldsymbol{n}^-\cdot\overline{\delta\boldsymbol{u}(\boldsymbol{x},\boldsymbol{w})}\,\mathrm{ds}. \qquad (8b)
\end{aligned}
$$

Furthermore, the abstract weak form (5) can be rewritten in a compact form for the solution vector $\boldsymbol{q}(\boldsymbol{x},\boldsymbol{w}) := \begin{pmatrix}\boldsymbol{\mathcal{A}}_\varepsilon^{AC}(\boldsymbol{x},\boldsymbol{w})\\ \boldsymbol{\mathcal{U}}^{AC}(\boldsymbol{x},\boldsymbol{w})\end{pmatrix}$ as: Find complex solutions $\boldsymbol{q} \in \tilde{X}_\Omega \times Y$ such that:

$$
\boldsymbol{a}(\boldsymbol{q}(\boldsymbol{x},\boldsymbol{w}), \delta\boldsymbol{q}(\boldsymbol{x},\boldsymbol{w})) = \boldsymbol{r}(\delta\boldsymbol{q}(\boldsymbol{x},\boldsymbol{w})), \qquad (9)
$$

for all $\delta\boldsymbol{q} \in \tilde{X}_\Omega \times Y$.

[5]Note that the sub-index ε in $\boldsymbol{A}_{\varepsilon,hq}^{DC}, \boldsymbol{\mathcal{A}}_{\varepsilon,hq}^{AC}$ is used to indicate that gauging by regularisation has been applied. See [39, 38, 23] for further details.

4 Discrete System: Full Order Solution

For the solution of the DC and AC problems, the finite element method is applied. A discrete Galerkin FE approximation is introduced and we approximate $\boldsymbol{u}^{DC}$ by $\boldsymbol{u}_{hp}^{DC}$ and $\boldsymbol{A}^{DC}$ by $\boldsymbol{A}_{\varepsilon,hq}^{DC}$ using high order H^1 and $\boldsymbol{H}(\text{curl})$ conforming elements [37], respectively. In the same manner, the AC fields are approximated by $\boldsymbol{\mathcal{A}}_{\varepsilon,hq}^{AC}, \boldsymbol{\mathcal{U}}_{hp}^{AC}$. Note that the sub-indices q and p denote the order of the $\boldsymbol{H}(\text{curl})$ and H^1 basis functions, respectively and h refers to the chosen mesh. Even though the discrete system combines two element types, it does not represent a saddle point problem, and thus we can be flexible with the degree of approximation p for $\boldsymbol{\mathcal{U}}_{hp}^{AC}$ and q for $\boldsymbol{\mathcal{A}}_{\varepsilon,hq}^{AC}$ [39]. In this work, the focus will be the application of POD to the AC system and thus only the discrete AC system is stated. For further details about the derivation of the DC and AC systems, we refer to [38, 39].

4.1 AC Discrete System

For parameters of interest $\boldsymbol{w}$, let us define the Galerkin FE approximation to the AC fields at position $\boldsymbol{x}$ as

$$\boldsymbol{q}_{hpq}(\boldsymbol{x},\boldsymbol{w}) := \begin{pmatrix} \boldsymbol{\mathcal{A}}_{\varepsilon,hq}^{AC}(\boldsymbol{x},\boldsymbol{w}) \\ \boldsymbol{\mathcal{U}}_{hp}^{AC}(\boldsymbol{x},\boldsymbol{w}) \end{pmatrix} = \begin{pmatrix} \sum_{i=1}^{P_{global}} \boldsymbol{N}^i(\boldsymbol{x}) \mathcal{A}_{\varepsilon}^{\mathrm{AC},i}(\boldsymbol{w}) \\ \sum_{i=1}^{Q_{global}} L^i(\boldsymbol{x})\, \boldsymbol{\mathcal{U}}^{\mathrm{AC},i}(\boldsymbol{w}) \end{pmatrix} \in S, \tag{10}$$

where $S := (\tilde{X}_\Omega \cap X_{hq}) \times (Y \cap Y_{hp})$, $\boldsymbol{N}^i(\boldsymbol{x})$ and $L^i(\boldsymbol{x})$ denote typical $\boldsymbol{H}(\text{curl})$ and H^1 basis functions, respectively and X_{hq} and Y_{hp} are defined as

$$X_{hq} := \text{span}\left\{\boldsymbol{N}^1, \boldsymbol{N}^2, \ldots, \boldsymbol{N}^{P_{global}}\right\},$$
$$Y_{hp} := \text{span}\left\{ \begin{pmatrix} L_1 \\ 0 \\ 0 \end{pmatrix}, \begin{pmatrix} 0 \\ L_1 \\ 0 \end{pmatrix}, \begin{pmatrix} 0 \\ 0 \\ L_1 \end{pmatrix}, \ldots, \begin{pmatrix} L_{Q_{global}} \\ 0 \\ 0 \end{pmatrix}, \begin{pmatrix} 0 \\ L_{Q_{global}} \\ 0 \end{pmatrix}, \begin{pmatrix} 0 \\ 0 \\ L_{Q_{global}} \end{pmatrix} \right\}.$$

Furthermore, $N_d = P_{global} + 3Q_{global}$ is the total number of degrees of freedom (DOF), which are split into P_{global} electromagnetic DOF and $3Q_{global}$ mechanical DOF and

$$\mathbf{N}(\boldsymbol{x}) := \left[\boldsymbol{N}^1, \boldsymbol{N}^2, \ldots, \boldsymbol{N}^{P_{global}}\right], \tag{11a}$$

$$\mathbf{L}(\boldsymbol{x}) := \left[\mathbf{l}_1, \mathbf{l}_2, \ldots, \mathbf{l}_{3Q_{global}}\right] = \begin{bmatrix} L^1 & 0 & 0 & \ldots & L^{Q_{global}} & 0 & 0 \\ 0 & L^1 & 0 & \ldots & 0 & L^{Q_{global}} & 0 \\ 0 & 0 & L^1 & \ldots & 0 & 0 & L^{Q_{global}} \end{bmatrix}, \tag{11b}$$

are the matrices of $\boldsymbol{H}(\text{curl})$ and H^1 basis functions, where $\mathbf{l}_1(\boldsymbol{x}), \mathbf{l}_2(\boldsymbol{x}), \ldots, \mathbf{l}_{3Q_{global}}(\boldsymbol{x})$ are the columns of $\mathbf{L}(\boldsymbol{x})$, so that

$$\boldsymbol{q}_{hpq}(\boldsymbol{x},\boldsymbol{w}) = \begin{pmatrix} \mathbf{N}(\boldsymbol{x})\boldsymbol{\mathcal{A}}_{\varepsilon}^{\mathrm{AC}}(\boldsymbol{w}) \\ \mathbf{L}(\boldsymbol{x})\boldsymbol{\mathcal{U}}^{\mathrm{AC}}(\boldsymbol{w}) \end{pmatrix} = \begin{bmatrix} \mathbf{N}(\boldsymbol{x}) & \mathbf{0} \\ \mathbf{0} & \mathbf{L}(\boldsymbol{x}) \end{bmatrix} \begin{pmatrix} \boldsymbol{\mathcal{A}}_{\varepsilon}^{\mathrm{AC}}(\boldsymbol{w}) \\ \boldsymbol{\mathcal{U}}^{\mathrm{AC}}(\boldsymbol{w}) \end{pmatrix} = \mathbf{O}(\boldsymbol{x})\mathbf{q}(\boldsymbol{w}), \tag{12}$$

where $\mathbf{o}_1(\boldsymbol{x}), \ldots, \mathbf{o}_{N_d}(\boldsymbol{x})$ are the columns of $\mathbf{O}(\boldsymbol{x})$ and $\mathbf{q}(\boldsymbol{w}) := \begin{pmatrix} \boldsymbol{\mathcal{A}}_{\varepsilon}^{\mathrm{AC}}(\boldsymbol{w}) \\ \boldsymbol{\mathcal{U}}^{\mathrm{AC}}(\boldsymbol{w}) \end{pmatrix}$. Note that here, and in the following, we use a Roman font for matrices and discrete quantities, while an Italic font is used for continuous vector fields and tensors. Inserting the discrete approximation to the solution field in the variational form (9) we obtain

$$\sum_{i=1}^{N_d} \sum_{j=1}^{N_d} \overline{\delta \mathrm{q}_i(\boldsymbol{w})} \boldsymbol{a}\left(\mathbf{o}_j(\boldsymbol{x}), \mathbf{o}_i(\boldsymbol{x})\right) \mathrm{q}_j(\boldsymbol{w}) = \sum_{i=1}^{N_d} \overline{\delta \mathrm{q}_i(\boldsymbol{w})} \boldsymbol{r}\left(\mathbf{o}_i(\boldsymbol{x})\right), \tag{13}$$

and, choosing $\delta \mathrm{q}_i(\boldsymbol{w})$ appropriately, this leads to the system of equations

$$\mathbf{A}(\boldsymbol{w})\mathbf{q}(\boldsymbol{w}) = \mathbf{R}(\boldsymbol{w}). \tag{14}$$

This is of size N_d and the system matrix and right hand side vector are defined as (see [38, 39])

$$\begin{aligned}\mathbf{A}(\boldsymbol{w}) &:= \begin{bmatrix}\mathbf{A}_{\mathcal{A}\mathcal{A}}(\boldsymbol{w}) & \mathbf{0}\\ \mathbf{A}_{\mathcal{U}\mathcal{A}}(\boldsymbol{w}) & \mathbf{A}_{\mathcal{U}\mathcal{U}}(\boldsymbol{w})\end{bmatrix}\\ &= \begin{bmatrix}\mathbf{K}^{\mathrm{AC}}_{\mathcal{A}\mathcal{A}}(\boldsymbol{w}) + \mathbf{C}^{\mathrm{AC}}_{\mathcal{A}\mathcal{A}}(\boldsymbol{w}) & \mathbf{0}\\ \mathbf{K}^{\mathrm{AC}}_{\mathcal{U}\mathcal{A}}(\boldsymbol{w}) & \mathbf{K}^{\mathrm{AC}}_{\mathcal{U}\mathcal{U}}(\boldsymbol{w}) + \mathrm{i}\omega\mathbf{C}^{\mathrm{AC}}_{\mathcal{U}\mathcal{U}}(\boldsymbol{w}) - \omega^2\mathbf{M}^{\mathrm{AC}}_{\mathcal{U}\mathcal{U}}(\boldsymbol{w})\end{bmatrix}, \qquad (15a)\\ \mathbf{R}(\boldsymbol{w}) &:= \begin{pmatrix}\mathbf{R}_{\mathcal{A}}(\boldsymbol{w})\\ \mathbf{0}\end{pmatrix} = \begin{pmatrix}\mathbf{R}^{\mathrm{AC}}_{\mathcal{A}}(\boldsymbol{w})\\ \mathbf{0}\end{pmatrix}. \qquad (15b)\end{aligned}$$

In the above, a mass proportional damping block $\mathbf{C}_{\mathcal{U}\mathcal{U}} = \alpha_M \mathbf{M}_{\mathcal{U}\mathcal{U}}$ has been added to the system as a first approximation to the physical damping present in a real MRI scanner. The mass proportional coefficient α_M is defined in terms of the angular frequency ω and the damping ratio ξ as $\alpha_M = 2\omega\xi$ [17]. Definitions of the blocks in the system above can be found in [38, 39].

5 Reduced Order Modelling

The design of a new MRI scanner requires the repeated solution of the magneto-mechanical problem (1) in order to investigate how the solution depends on parameters of interest, including frequency and conductivity of each shield among others. Although an accurate and efficient methodology for the solution of the full order problem was presented in [39], this leads, in an industrial environment, to a bottleneck in terms of computational cost, since, each time a given parameter is modified, a system of size N_d must be solved, making the whole process extremely expensive. In light of this, the application of ROM techniques that help reduce the design time of new MRI configurations is considered.

5.1 The Proper Orthogonal Decomposition

To obtain a reduced basis for $\mathbf{q}(\boldsymbol{w})$ in (14), we apply POD and, in the following, we focus only on the discrete POD version (also referred to as PCA in the literature [8, 29]). Its main objective is, given a high dimensional set of data, to find the optimal basis (or principal components) to reproduce the data in a lower dimensional space, while retaining as much as possible of the variation present in the data set.

5.1.1 Off-line Stage: Construction of the Basis via SVD

The solution coefficients $\mathbf{q}(\boldsymbol{w})$ in (14) are approximated in separate format as

$$\mathbf{q}(\boldsymbol{w}) \approx \sum_{k=1}^{N} \mathrm{a}_k(\boldsymbol{w})\boldsymbol{\phi}_k, \qquad (16)$$

for some basis vectors $\boldsymbol{\phi}_k$ and parameter dependent amplitudes $\mathrm{a}_k(\boldsymbol{w})$, with a small number of terms $N << N_d$. The first goal is to find a suitable set of $\boldsymbol{\phi}_k$ that spans the variation of $\mathbf{q}$ with $\boldsymbol{w}$. To achieve this, a set of snapshots is computed, aiming at sampling the family of solutions $\mathbf{q}$ when $\boldsymbol{w}$ changes [8, 9]. The computation of each snapshot involves the computation of one full order problem. A matrix of snapshots $\mathbf{D} \in \mathbb{C}^{N_d \times N_s}$ is built in the form [6]

$$\mathbf{D} = \left[\mathbf{q}(\mathbf{w}_1), \quad \mathbf{q}(\mathbf{w}_2), \quad \ldots, \quad \mathbf{q}(\mathbf{w}_{N_s})\right], \qquad (17)$$

where $\mathbf{q}(\mathbf{w}_j)$ is a single snapshot obtained as the solution to (14) for a given set of parameters $\mathbf{w}_j$[7] and N_s is the number of computed snapshots.

[6] Note that for our application $N_d > N_s$ and thus, for the sake of simplicity, we will restrict our consideration to this case.

[7] Note that the roman font in $\mathbf{w}$ is used to denote a discrete set of sampled parameters.

In order to obtain the optimal basis $\boldsymbol{\phi}_k$ to represent this data, the singular value decomposition (SVD) [6, 15] can be applied, leading to the representation of the snapshot matrix

$$\mathbf{D} = \mathbf{H}\boldsymbol{\Sigma}\mathbf{G}^* = \sum_{k=1}^{N_s} \mathbf{h}_k \sigma_k \left(\mathbf{g}_k\right)^* , \tag{18}$$

where $\mathbf{H} = [\mathbf{h}_1, \ldots, \mathbf{h}_m] \in \mathbb{C}^{N_d \times N_d}$ and $\mathbf{G} = [\mathbf{g}_1, \ldots, \mathbf{g}_n] \in \mathbb{C}^{N_s \times N_s}$ are unitary matrices containing the left and right singular vectors of $\mathbf{D}$, respectively, $\mathbf{G}^*$ denotes the complex conjugate transpose of $\mathbf{G}$, $\boldsymbol{\Sigma} \in \mathbb{R}^{N_d \times N_s}$ is the matrix $\boldsymbol{\Sigma} = \begin{bmatrix} \boldsymbol{\Sigma}_r & \mathbf{0} \\ \mathbf{0} & \mathbf{0} \end{bmatrix}$ with $\boldsymbol{\Sigma}_r = \mathrm{diag}(\sigma_1, ..., \sigma_r)$, being r the rank of $\mathbf{D}$ and $\sigma_1 \geqslant \sigma_2 \geqslant \cdots \geqslant \sigma_r > 0$ are the singular values of $\mathbf{D}$. The solution for any sampled parameters $\mathbf{w}_j$ can then be recovered, if desired, using

$$\mathbf{q}(\mathbf{w}_j) = \sum_{k=1}^{N_s} \mathbf{h}_k \sigma_k \overline{\mathrm{g}_{jk}} = \mathbf{H}\boldsymbol{\Sigma} \left(\mathbf{G}^*\right)_j , \tag{19}$$

where g_{jk} is the entry of $\mathbf{G}$ at the j-th row and k-th column, the optimal set of basis $\boldsymbol{\phi}_k$ have been found to be $\mathbf{h}_k$ and the amplitudes $\mathrm{a}_k(\mathbf{w}_j)$ have been found to be $\sigma_k \overline{\mathrm{g}_{jk}}$. Note that the notation $\left(\mathbf{G}^*\right)_j$ is used to denote the j-th column of $\mathbf{G}^*$ and the dependency on $\mathbf{w}_j$ is emphasized trough the sub-index j.
Two points should be noted. First, the size of the basis in (19) is N_s. Second, the SVD provides the amplitudes σ_k in decreasing order. Therefore, it is usual to truncate the sum in (19), that is, further reduced the basis neglecting all the modes with σ_k smaller than a given tolerance [6, 15, 21]. This process is usually referred as Truncated Singular Value Decomposition (TSVD), and the truncated approximation then reads,

$$\mathbf{D} \approx \mathbf{D}^M := \sum_{k=1}^{M} \mathbf{h}_k \sigma_k \left(\mathbf{g}_k\right)^* = \mathbf{H}^M \boldsymbol{\Sigma}^M \left(\mathbf{G}^M\right)^* , \tag{20}$$

where the contributions from the smallest singular values have been filtered and only the largest $M < N_s$ singular values have been retained, which is denoted by the superscript M. The left singular vectors can then be arranged in a matrix $\mathbf{H}^M \in \mathbb{C}^{N_d \times M}$, the right singular vectors in a matrix $\mathbf{G}^M \in \mathbb{C}^{N_s \times M}$ and the singular values are the diagonal entries in the matrix $\boldsymbol{\Sigma}^M \in \mathbb{R}^{M \times M}$. The rank M of the approximated matrix is also referred to as the number of modes.
The solution, for a sampled parameter set, can then be approximated using

$$\mathbf{q}(\mathbf{w}_j) \approx \mathbf{q}^{\mathrm{POD}}(\mathbf{w}_j) := \sum_{k=1}^{M} \mathbf{h}_k \sigma_k \overline{\mathrm{g}_{jk}} = \mathbf{H}^M \boldsymbol{\Sigma}^M \left(\left(\mathbf{G}^M\right)^*\right)_j , \tag{21}$$

where, comparing with (16), $\mathrm{a}_k(\mathbf{w}_j) = \sigma_k \overline{\mathrm{g}_{jk}}$, $\boldsymbol{\phi}_k = \mathbf{h}_k$ and $N = M$.
The process of computing the snapshots and applying the TSVD is usually referred to as *off-line* stage, as this can be computed and stored at an initial stage independently of sweeps of the parameters of interest $\boldsymbol{w}$. This *off-line* stage is summarised in Algorithm 1, where $\mathbf{W}_\mathrm{s} := (\mathbf{w}_1, \mathbf{w}_2, \ldots, \mathbf{w}_{N_s})$ denotes the chosen samples. Note that the input arguments $\mathbf{A}(\boldsymbol{w}), \mathbf{R}(\boldsymbol{w})$ in the algorithm indicate that we are giving the algorithm a method to compute $\mathbf{A}$ and $\mathbf{R}$ for all $\boldsymbol{w}$. This can be done by assembling the system for each new parameter set, or using an affine decomposition, if available, as described in Appendix A.
Our aim is to construct an approximated solution $\mathbf{q}^{\mathrm{POD}}(\boldsymbol{w})$ for any $\boldsymbol{w}$, not just for the sampled values. This is done in the so-called *on-line* stage, where two different approaches, namely PODI and PODP, can be used to obtain $\mathbf{q}^{\mathrm{POD}}(\boldsymbol{w})$ for any value of $\boldsymbol{w}$ [44]. PODI [34, 33, 7] is less intrusive than PODP [40, 13, 12] since it does not require any information from the finite element solver, as opposed to PODP, which requires the FE system matrices to be accessible. On the other hand, PODI requires the solution to have a smooth variation with the parameters in order to provide accurate results, while PODP offers an increased accuracy and robustness, especially as the smoothness of the solution decreases [44, 36]. These approaches are described in the next two subsections.

Algorithm 1 Off-line Stage

function OFFLINE($\mathbf{A}(\boldsymbol{w}), \mathbf{R}(\boldsymbol{w}), \mathbf{W}_s, M$)
  for $\mathbf{w}_s \in \mathbf{W}_s$ **do**
    Find $\mathbf{q}(\mathbf{w}_s)$ such that
    $\mathbf{A}(\mathbf{w}_s)\mathbf{q}(\mathbf{w}_s) = \mathbf{R}(\mathbf{w}_s)$
  end for
  Build snapshot matrix $\mathbf{D} = [\mathbf{q}(\mathbf{w}_1), \mathbf{q}(\mathbf{w}_2), \ldots, \mathbf{q}(\mathbf{w}_{N_s})]$
  Apply TSVD to get $\mathbf{D} \approx \mathbf{D}^M = \mathbf{H}^M \boldsymbol{\Sigma}^M \left(\mathbf{G}^M\right)^*$
  return $\mathbf{H}^M, \boldsymbol{\Sigma}^M, \mathbf{G}^M$
end function

5.1.2 On-line Interpolation Based POD (PODI)

Expression (21) describes how the POD solution $\mathbf{q}(\mathbf{w}_j)$ can be recovered from a TSVD when $\boldsymbol{w} = \mathbf{w}_j$ is a set of parameters that has been sampled. In PODI, the coefficients $\overline{\mathrm{g}_{jk}}$ are interpolated in order to obtain the solution at others parameters of interest. This solution takes the form

$$\mathbf{q}^{\mathrm{PODI}}(\boldsymbol{w}) := \sum_{k=1}^{M} \mathbf{h}_k \sigma_k \sum_{j=1}^{M} I_j(\boldsymbol{w}) \overline{\mathrm{g}_{jk}}, \tag{22}$$

where $I_j(\boldsymbol{w})$ denote a certain set of interpolation functions, whose definitions can change depending on $\boldsymbol{w}$. The simple case of Lagrange linear and cubic interpolation will be considered and compared later in this work, although (22) also holds for arbitrary high order Lagrange interpolation. We do not consider such approximations here as it is well known that this can lead to additional oscillations in the interpolated solution e.g. [41]. Furthermore, when considering arbitrary high dimensional spaces, this interpolation becomes challenging due to the necessity to use dense meshes and ensure a properly posed set of nodes is chosen [24]. Due to this, it is difficult, in general, to find an interpolation scheme that is both accurate and efficient for the case of an arbitrary high dimensional space [20]. Hence, the application of PODI is, in general, better suited when the number of parameters of interest is small, and becomes more challenging when N_p is large. Note that more complex techniques, such as the interpolation on Grassmann manifolds, have been considered in the literature [1, 30, 43] demonstrating, for certain applications, a superior accuracy compared to classical interpolation techniques. The interpolation chosen in this work is the simplest choice and interpolation on Grassmann manifolds has the potential to offer an increased accuracy.
The *on-line* PODI stage is summarised in algorithmic format in Algorithm 2, which results in the output $\boldsymbol{q}^{PODI}(\boldsymbol{x}, \boldsymbol{w}) \in S$.

Algorithm 2 On-Line PODI Stage

function ONLINEPODI($\mathbf{H}^M, \boldsymbol{\Sigma}^M, \mathbf{G}^M, \mathbf{O}, M, \boldsymbol{x}, \boldsymbol{w}$)
  $\mathbf{q}^{\mathrm{PODI}}(\boldsymbol{w}) = \sum_{k=1}^{M} \mathbf{h}_k \sigma_k \sum_{j=1}^{M} I_j(\boldsymbol{w}) \overline{\mathrm{g}_{jk}}$
  $\boldsymbol{q}^{PODI}(\boldsymbol{x}, \boldsymbol{w}) = \mathbf{O}(\boldsymbol{x}) \mathbf{q}^{\mathrm{PODI}}(\boldsymbol{w})$
  return $\boldsymbol{q}^{PODI}(\boldsymbol{x}, \boldsymbol{w})$
end function

5.1.3 On-line Projection Based POD (PODP)

In the projection approach, the singular values and right singular vectors obtained from the TSVD are neglected, and the solution is approximated as a linear combination of the left singular vectors or basis vectors in the form

$$\mathbf{q}^{\mathrm{PODP}}(\boldsymbol{w}) := \sum_{k=1}^{M} \mathbf{h}_k \mathrm{p}_k(\boldsymbol{w}) = \mathbf{H}^M \mathbf{p}(\boldsymbol{w}), \tag{23}$$

where the parametric mode vector $\mathbf{p}(\boldsymbol{w})$ is unknown. Inserting this approximation into expression (12), the solution $\boldsymbol{q}_{hpq}(\boldsymbol{x}, \boldsymbol{w})$ can be approximated using

$$\boldsymbol{q}_{hpq}(\boldsymbol{x}, \boldsymbol{w}) \approx \boldsymbol{q}^{PODP}(\boldsymbol{x}, \boldsymbol{w}) := \mathbf{O}(\boldsymbol{x})\mathbf{q}^{\mathrm{PODP}}(\boldsymbol{w}) = \mathbf{O}(\boldsymbol{x}) \sum_{k=1}^{M} \mathbf{h}_k \mathrm{p}_k(\boldsymbol{w}) \in S. \tag{24}$$

Then, substituting (24) into the weak form (9) and choosing to approximate the test functions $\delta\boldsymbol{q}$ in the same manner, the next expression is obtained

$$\sum_{i=1}^{M}\sum_{j=1}^{M} \overline{\delta \mathrm{p}_i(\boldsymbol{w})}\boldsymbol{a}\left(\mathbf{O}(\boldsymbol{x})\mathbf{h}_j, \mathbf{O}(\boldsymbol{x})\mathbf{h}_i\right) \mathrm{p}_j(\boldsymbol{w}) = \sum_{i=1}^{M} \overline{\delta \mathrm{p}_i(\boldsymbol{w})}\boldsymbol{r}\left(\mathbf{O}(\boldsymbol{x})\mathbf{h}_i\right), \tag{25}$$

and, choosing $\delta \mathrm{p}_i(\boldsymbol{w})$ appropriately, this leads to the reduced linear system

$$\left[\left(\mathbf{H}^M\right)^* \mathbf{A}(\boldsymbol{w})\mathbf{H}^M\right] \mathbf{p}(\boldsymbol{w}) = \left(\mathbf{H}^M\right)^* \mathbf{R}(\boldsymbol{w}), \tag{26}$$

that is of size M. Once system (26) is solved, the solution $\boldsymbol{q}^{PODP}(\boldsymbol{x}, \boldsymbol{w})$ can be obtained from expression (24).

Defining the reduced matrix of the system, obtained by projection onto the reduced dimension space, as $\mathbf{A}^M(\boldsymbol{w}) := \left(\mathbf{H}^M\right)^* \mathbf{A}\mathbf{H}^M$ and the reduced right hand side vector as $\mathbf{R}^M(\boldsymbol{w}) := \left(\mathbf{H}^M\right)^* \mathbf{R}(\boldsymbol{w})$, equation (26) becomes

$$\mathbf{A}^M(\boldsymbol{w})\mathbf{p}(\boldsymbol{w}) = \mathbf{R}^M(\boldsymbol{w}). \tag{27}$$

Note that the coefficients in the solution vector $\mathbf{p}(\boldsymbol{w})$ define the ROM approximation and are obtained by solving a system of size M, which is computationally much cheaper than the full order problem when $M << N_d$. The *on-line* PODP stage is summarised in algorithmic format in Algorithm 3, which has as output $\boldsymbol{q}^{PODP}(\boldsymbol{x}, \boldsymbol{w}) \in S$.

Algorithm 3 On-Line PODP Stage

1: **function** ONLINEPODP($\mathbf{H}^M, \mathbf{A}^M(\boldsymbol{w}), \mathbf{R}^M(\boldsymbol{w}), \mathbf{O}, \boldsymbol{x}, \boldsymbol{w}$)
2: Find $\mathbf{p}(\boldsymbol{w})$ such that
$\mathbf{A}^M(\boldsymbol{w})\mathbf{p}(\boldsymbol{w}) = \mathbf{R}^M(\boldsymbol{w})$
3: $\mathbf{q}^{\mathrm{PODP}}(\boldsymbol{w}) = \mathbf{H}^M\mathbf{p}(\boldsymbol{w})$
4: $\boldsymbol{q}^{PODP}(\boldsymbol{x}, \boldsymbol{w}) = \mathbf{O}(\boldsymbol{x})\mathbf{q}^{\mathrm{PODP}}(\boldsymbol{w})$
5: **return** $\boldsymbol{q}^{PODP}(\boldsymbol{x}, \boldsymbol{w})$
6: **end function**

PODP has the advantage that the POD solution is still forced to obey the equation of the problem in its reduced form (26) for all $\boldsymbol{w}$, while in PODI we simply interpolate the parameter dependent amplitudes. This usually leads to a higher accuracy and robustness [44] of PODP compared to PODI, but it also has the increased cost of having to build and solve the small system (26). Note that computing the products $\left(\mathbf{H}^M\right)^* \mathbf{A}(\boldsymbol{w})\mathbf{H}^M$ and $\left(\mathbf{H}^M\right)^* \mathbf{R}(\boldsymbol{w})$ is expensive and, thus, we want to avoid computing it for each new value of $\boldsymbol{w}$. For this purpose, an affine decomposition in terms of the parameters of interest is usually developed [16], where the system matrix is expressed in terms of some modified matrices that are independent of $\boldsymbol{w}$ and parameter dependent scalar coefficients that multiply this matrices. In particular, our problem of interest admits an exact affine decomposition in terms of frequency and conductivity, which leads to a much faster *on-line* PODP stage. For details about the derivation of this affine decomposition see Appendix A.

5.2 Application to Separated Physics

Given that the formulation proposed in Section 2 results in a staggered scheme, the proposed ROMs can be applied to the complete coupled problem or to each one of the physics separately. In this section we summarize the steps needed at the *off-line* and *on-line* stages when considering application to the separated physics.

Off-line

In the *off-line* stage, Algorithm 1 is applied to both physics separately. For this, we first consider $\boldsymbol{q}(\boldsymbol{x},\boldsymbol{w}) = \boldsymbol{\mathcal{A}}_{\varepsilon}^{AC}(\boldsymbol{x},\boldsymbol{w})$ and then call OFFLINE$(\mathbf{A}_{\mathcal{A}\mathcal{A}}(\boldsymbol{w}), \mathbf{R}_{\mathcal{A}}(\boldsymbol{w}), \mathbf{W}_{\mathrm{s}}, M)$ to obtain the low rank approximation $\mathbf{D}_{\mathcal{A}}^{M} = \mathbf{H}_{\mathcal{A}}^{M}\boldsymbol{\Sigma}_{\mathcal{A}}^{M}\left(\mathbf{G}_{\mathcal{A}}^{M}\right)^{*}$ to the snapshot matrix $\mathbf{D}_{\mathcal{A}}$. Secondly, we then consider $\boldsymbol{q}(\boldsymbol{x},\boldsymbol{w}) = \boldsymbol{\mathcal{U}}^{AC}(\boldsymbol{x},\boldsymbol{w})$ and then call OFFLINE$(\mathbf{A}_{\mathcal{U}\mathcal{U}}(\boldsymbol{w}), -\mathbf{A}_{\mathcal{U}\mathcal{A}}(\boldsymbol{w})\boldsymbol{\mathcal{A}}_{\varepsilon}^{\mathrm{AC}}(\boldsymbol{w}), \mathbf{W}_{\mathrm{s}}, M)$ to obtain the low rank approximation $\mathbf{D}_{\mathcal{U}}^{M} = \mathbf{H}_{\mathcal{U}}^{M}\boldsymbol{\Sigma}_{\mathcal{U}}^{M}\left(\mathbf{G}_{\mathcal{U}}^{M}\right)^{*}$ to the snapshot matrix $\mathbf{D}_{\mathcal{U}}$. Note that the application to separated physics offers extra flexibility, as different N_s and M can be considered for each physics, if desired.

On-line

In the *on-line* stage, either PODI or PODP can be considered. If we choose to apply PODI, the *on-line* stage for electromagnetics then consists in calling ONLINEPODI$(\mathbf{H}_{\mathcal{A}}^{M}, \boldsymbol{\Sigma}_{\mathcal{A}}^{M}, \mathbf{G}_{\mathcal{A}}^{M}, \mathbf{N}, M, \boldsymbol{x}, \boldsymbol{w})$ (Algorithm 2) to get the approximation $\boldsymbol{\mathcal{A}}^{PODI}(\boldsymbol{x},\boldsymbol{w})$ to $\boldsymbol{\mathcal{A}}_{\varepsilon,hq}^{AC}(\boldsymbol{x},\boldsymbol{w})$. For mechanics, the *on-line* stage consists in calling ONLINEPODI$(\mathbf{H}_{\mathcal{U}}^{M}, \boldsymbol{\Sigma}_{\mathcal{U}}^{M}, \mathbf{G}_{\mathcal{U}}^{M}, \mathbf{L}, M, \boldsymbol{x}, \boldsymbol{w})$ to get the approximation $\boldsymbol{\mathcal{U}}^{PODI}(\boldsymbol{x},\boldsymbol{w})$ to $\boldsymbol{\mathcal{U}}_{hp}^{AC}(\boldsymbol{x},\boldsymbol{w})$. If we choose instead to apply PODP, the *on-line* stage for electromagnetics then consists in calling ONLINEPODP$(\mathbf{H}_{\mathcal{A}}^{M}, \left(\mathbf{H}_{\mathcal{A}}^{M}\right)^{*}\mathbf{A}_{\mathcal{A}\mathcal{A}}(\boldsymbol{w})\mathbf{H}_{\mathcal{A}}^{M}, \left(\mathbf{H}_{\mathcal{A}}^{M}\right)^{*}\mathbf{R}_{\mathcal{A}}(\boldsymbol{w}), \mathbf{N}, \boldsymbol{x}, \boldsymbol{w})$ (Algorithm 3) to obtain the approximation $\boldsymbol{\mathcal{A}}^{PODP}(\boldsymbol{x},\boldsymbol{w})$ to $\boldsymbol{\mathcal{A}}_{\varepsilon,hq}^{AC}(\boldsymbol{x},\boldsymbol{w})$, and subsequently, for mechanics we call ONLINEPODP$(\mathbf{H}_{\mathcal{U}}^{M}, \left(\mathbf{H}_{\mathcal{U}}^{M}\right)^{*}\mathbf{A}_{\mathcal{U}\mathcal{U}}(\boldsymbol{w})\mathbf{H}_{\mathcal{U}}^{M}, \left(\mathbf{H}_{\mathcal{U}}^{M}\right)^{*}\left(-\mathbf{A}_{\mathcal{U}\mathcal{A}}(\boldsymbol{w})\boldsymbol{\mathcal{A}}_{\varepsilon}^{\mathrm{AC}}(\boldsymbol{w})\right), \mathbf{L}, \boldsymbol{x}, \boldsymbol{w})$ to obtain the approximation $\boldsymbol{\mathcal{U}}^{PODP}(\boldsymbol{x},\boldsymbol{w})$ to $\boldsymbol{\mathcal{U}}_{hp}^{AC}(\boldsymbol{x},\boldsymbol{w})$.[8]

5.3 Combined Reduced Order-Full Order Approach

The different ROMs proposed in this work are written in terms of a general set of parameters $\boldsymbol{w}$. However, it is important to note that for our application, the interest lies typically in predicting the evolution of certain magnitudes such as dissipated power and kinetic energy (defined later in (31)) with frequency for different material parameters. Thus, frequency is in general one of the most important parameters in our problem. Figures (3a) and (3b) show the evolution with frequency of $||\boldsymbol{\mathcal{A}}_{\varepsilon,hq}^{AC}||_{L^2(\Omega_{C,n})}$ and $||\boldsymbol{\mathcal{U}}_{hp}^{AC}||_{L^2(\Omega_{C,n})}$, where $\Omega_{C,n}$ refers to either Ω_{4K}, Ω_{77K} or Ω_{OVC}, for a simplified MRI configuration obtained by performing a full order simulation [39]. The critical observation is that peaks appear only in $||\boldsymbol{\mathcal{U}}_{hp}^{AC}||_{L^2(\Omega_{C,n})}$, and not in $||\boldsymbol{\mathcal{A}}_{\varepsilon,hq}^{AC}||_{L^2(\Omega_{C,n})}$, the latter exhibiting a smooth monotonically decay and therefore, being well suited to a POD approximation. Moreover, this typical behaviour will always be the case for our application of interest where the peaks are associated with the resonance modes of the mechanical system, which will be activated depending on the induced electromagnetic stress $\boldsymbol{\sigma}^{e}(\boldsymbol{A})$. These resonant modes represent a problem for the application of POD, in particular in order to ensure that a set of snapshots that properly describes the variation of $\mathbf{q}$ with $\boldsymbol{w}$ is chosen, given that in the resonance frequencies, the system presents a singular behaviour that cannot be captured unless it is sampled. This suggests that the application of a novel combined reduced order-full order methodology in which POD is applied to the electromagnetic problem only and the mechanical problem is solved using the full order solver could be beneficial, as the electromagnetic solution should be easier to approximate with fewer snapshots and modes. Furthermore, $3Q_{global} \ll P_{global}$, which means the cost of the full order mechanical solver is much cheaper than that of full order electromagnetic solver.

Off-line

In the *off-line* stage, Algorithm 1 is applied to the electromagnetic problem only, ie we consider $\boldsymbol{q}(\boldsymbol{x},\boldsymbol{w}) = \boldsymbol{\mathcal{A}}_{\varepsilon}^{AC}(\boldsymbol{x},\boldsymbol{w})$ and then call OFFLINE$(\mathbf{A}_{\mathcal{A}\mathcal{A}}(\boldsymbol{w}), \mathbf{R}_{\mathcal{A}}(\boldsymbol{w}), \mathbf{W}_{\mathrm{s}}, M)$ to obtain the low rank approximation $\mathbf{D}_{\mathcal{A}}^{M} = \mathbf{H}_{\mathcal{A}}^{M}\boldsymbol{\Sigma}_{\mathcal{A}}^{M}\left(\mathbf{G}_{\mathcal{A}}^{M}\right)^{*}$ to the snapshot matrix $\mathbf{D}_{\mathcal{A}}$.

[8] Note that PODI can be applied independently to both physics, however in the case of PODP the application to mechanics requires, in practice, the method to be first applied to electromagnetics given that $\tilde{l}_{\mathcal{U}}$ depends on $\boldsymbol{\mathcal{A}}_{\varepsilon}^{AC}(\boldsymbol{x},\boldsymbol{w})$.

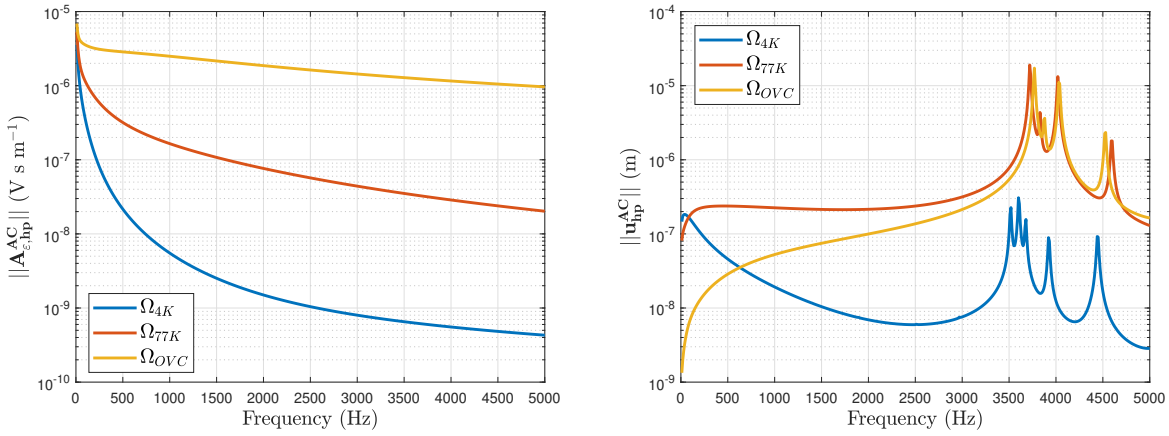

(a) $||\boldsymbol{\mathcal{A}}^{AC}_{\varepsilon,hq}||_{L^2(\Omega_{C,n})}$ (b) $||\boldsymbol{\mathcal{U}}^{AC}_{hp}||_{L^2(\Omega_{C,n})}$

Figure 3: Evolution of (a) $||\boldsymbol{\mathcal{A}}^{AC}_{\varepsilon,hq}||_{L^2(\Omega_{C,n})}$ and (b) $||\boldsymbol{\mathcal{U}}^{AC}_{hp}||_{L^2(\Omega_{C,n})}$ with the frequency for a simplified MRI problem (Test magnet problem).

On-line

In the on-line stage, the solution $\boldsymbol{\mathcal{A}}^{AC}_{\varepsilon,hq}$ for the parameters of interest can be approximated through PODI or PODP, and this is then used to feed the mechanical full order solver. For clarity, we use PODI-Full and PODP-Full to denote the *on-line* stage using PODI and PODP, respectively. For PODI-Full, we apply Algorithm 4 to obtain an approximation $\boldsymbol{q}^{PODI-FULL}(\boldsymbol{x},\boldsymbol{w})$ to $\boldsymbol{q}_{hpq}(\boldsymbol{x},\boldsymbol{w})$, and, for PODP-Full, we apply Algorithm 5 to obtain an approximation $\boldsymbol{q}^{PODP-FULL}(\boldsymbol{x},\boldsymbol{w})$ to $\boldsymbol{q}_{hpq}(\boldsymbol{x},\boldsymbol{w})$.

Algorithm 4 Combined PODI-Full

function ONLINEPODI-FULL($\mathbf{H}^M_A, \boldsymbol{\Sigma}^M_{\mathcal{A}}, \mathbf{G}^M_{\mathcal{A}}, \mathbf{A}_{\mathcal{U}\mathcal{U}}(\boldsymbol{w}), \mathbf{A}_{\mathcal{U}\mathcal{A}}(\boldsymbol{w}), \mathbf{N}, \mathbf{L}, M, \boldsymbol{x}, \boldsymbol{w}$)
  $\boldsymbol{\mathcal{A}}^{PODI}(\boldsymbol{x},\boldsymbol{w}) = $ ONLINEPODI($\mathbf{H}^M_{\mathcal{A}}, \boldsymbol{\Sigma}^M_{\mathcal{A}}, \mathbf{G}^M_{\mathcal{A}}, \mathbf{N}, M, \boldsymbol{x}, \boldsymbol{w}$)
  Find $\boldsymbol{\mathcal{U}}^{\mathrm{AC}}(\boldsymbol{w})$ such that
  $\mathbf{A}_{\mathcal{U}\mathcal{U}}(\boldsymbol{w})\boldsymbol{\mathcal{U}}^{\mathrm{AC}}(\boldsymbol{w}) = -\mathbf{A}_{\mathcal{U}\mathcal{A}}(\boldsymbol{w})\boldsymbol{\mathcal{A}}^{\mathrm{PODI}}(\boldsymbol{w})$
  $\boldsymbol{\mathcal{U}}^{AC}_{hp}(\boldsymbol{x},\boldsymbol{w}) = \mathbf{L}(\boldsymbol{x})\boldsymbol{\mathcal{U}}^{\mathrm{AC}}(\boldsymbol{w})$
  return $\boldsymbol{q}^{PODI-FULL}(\boldsymbol{x},\boldsymbol{w}) = \begin{pmatrix} \boldsymbol{\mathcal{A}}^{PODI}(\boldsymbol{x},\boldsymbol{w}) \\ \boldsymbol{\mathcal{U}}^{AC}_{hp}(\boldsymbol{x},\boldsymbol{w}) \end{pmatrix}$
end function

Algorithm 5 Combined PODP-Full

function ONLINEPODP-FULL($\mathbf{H}^M_A, \mathbf{A}(\boldsymbol{w}), \mathbf{R}(\boldsymbol{w}), \mathbf{N}, \mathbf{L}, \boldsymbol{x}, \boldsymbol{w}$)
  $\boldsymbol{\mathcal{A}}^{PODP}(\boldsymbol{x},\boldsymbol{w}) = $ ONLINEPODP($\mathbf{H}^M_{\mathcal{A}}, \left(\mathbf{H}^M_A\right)^* \mathbf{A}_{\mathcal{A}\mathcal{A}}(\boldsymbol{w})\mathbf{H}^M_A, \left(\mathbf{H}^M_A\right)^* \mathbf{R}_{\mathcal{A}}(\boldsymbol{w}), \mathbf{N}, \boldsymbol{x}, \boldsymbol{w}$)
  Find $\boldsymbol{\mathcal{U}}^{\mathrm{AC}}(\boldsymbol{w})$ such that
  $\mathbf{A}_{\mathcal{U}\mathcal{U}}(\boldsymbol{w})\boldsymbol{\mathcal{U}}^{\mathrm{AC}}(\boldsymbol{w}) = -\mathbf{A}_{\mathcal{U}\mathcal{A}}(\boldsymbol{w})\boldsymbol{\mathcal{A}}^{\mathrm{PODP}}(\boldsymbol{w})$
  $\boldsymbol{\mathcal{U}}^{AC}_{hp}(\boldsymbol{x},\boldsymbol{w}) = \mathbf{L}(\boldsymbol{x})\boldsymbol{\mathcal{U}}^{\mathrm{AC}}(\boldsymbol{w})$
  return $\boldsymbol{q}^{PODP-FULL}(\boldsymbol{x},\boldsymbol{w}) = \begin{pmatrix} \boldsymbol{\mathcal{A}}^{PODP}(\boldsymbol{x},\boldsymbol{w}) \\ \boldsymbol{\mathcal{U}}^{AC}_{hp}(\boldsymbol{x},\boldsymbol{w}) \end{pmatrix}$
end function

5.4 Error Measure

When considering the solution to our problem using a ROM an approximation error is introduced. To quantify this error, two measures will be considered. First, the relative truncation error introduced by truncating the SVD after M terms is quantified using [6]

$$||\mathbf{D} - \mathbf{D}^M||_F := \sqrt{\sum_{i=M+1}^{r} \sigma_i^2}, \tag{28}$$

where r is the rank of $\mathbf{D}$. However, this requires the complete SVD, which is generally not available and instead only a rank M approximation to $\mathbf{D}$ is available for computational efficiency. Thus, an upper bound e_1 is used [18]

$$\frac{||\mathbf{D} - \mathbf{D}^M||_F}{||\mathbf{D}||_F} = \frac{\sqrt{\sum_{i=M+1}^{r} \sigma_i^2}}{\sqrt{\sum_{i=1}^{r} \sigma_i^2}} \leqslant e_1 := \frac{\sqrt{(r-M)\sigma_M^2}}{\sqrt{\sum_{i=1}^{M} \sigma_i^2}}, \tag{29}$$

where the singular values are sorted in decreasing order and, therefore, $\sigma_M \geqslant \sigma_i$ for $M+1 \leqslant i \leqslant r$.
The second error measure represents the error of the reduced order solution with respect to the full order solution. To construct this measure, the solution to the problem for parameter values that have not been sampled is computed using both the full order and the ROM and the error is then defined for each parameter set $\boldsymbol{w}$ as

$$e_2(\mathbf{q}(\boldsymbol{w}), \mathbf{q}^{\text{POD}}(\boldsymbol{w})) := \frac{||\mathbf{q}(\boldsymbol{w}) - \mathbf{q}^{\text{POD}}(\boldsymbol{w})||_{N_d}}{||\mathbf{q}(\boldsymbol{w})||_{N_d}}, \tag{30}$$

where $||\cdot||_{N_d}$ is the N_d-dimensional Euclidean norm.

6 Results

The application of the discussed methodologies to challenging MRI configurations is now considered in order to study their accuracy and efficiency. Two different configurations, considering longitudinal as well as transversal gradient coils, will be studied, and comparisons against the full order solution will be provided.

6.1 Test Magnet Problem with 1 Parameter

In this section, a problem consisting of a simplified magnet configuration is considered. The full order model corresponding to this problem has been previously simulated in [39], and it basically consists of a set of main coils that generate a static magnetic field, a set of gradient coils that generate a transient magnetic field and three conducting radiation shields (4K, 77K and OVC). Note that only the longitudinal z gradient coils are considered in this case. An illustration of the geometry is shown in Figure 4, where the main coils are shown in red, the gradient coils in blue, and the different radiation shields (4K, 77K and OVC) in different green tones. Note that the 3D geometry (Figure 4b), can be obtained by rotating the $r-z$ plane (Figure 4a), through $0 \leqslant \phi < 2\pi$ rad about the z axis (where (r, ϕ, z) are cylindrical coordinates). The material parameters and loading conditions are the same as in [39], to which we refer for further details. Mechanical damping was applied as described in Section 4 with a damping ratio $\xi = 2 \times 10^{-3}$. For the finite element discretisation, a mesh of 33 805 tetrahedral elements and polynomial orders $p = 3$ and $q = 3$ were considered. As a first study, $\omega = 2\pi f$ is considered as the only parameter. Thus, $N_p = 1$ and $\boldsymbol{w}$ reduces to ω.

6.1.1 POD Applied to Complete Physics Solutions

The purpose of this section is to show the inefficiencies of a naive approach based on applying PODI and PODP to the complete physics problem (14) for the test magnet example.

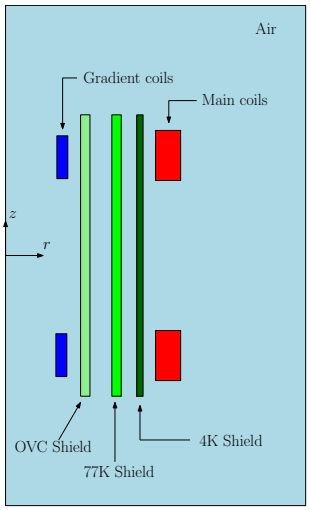

(a) 2D crosssection

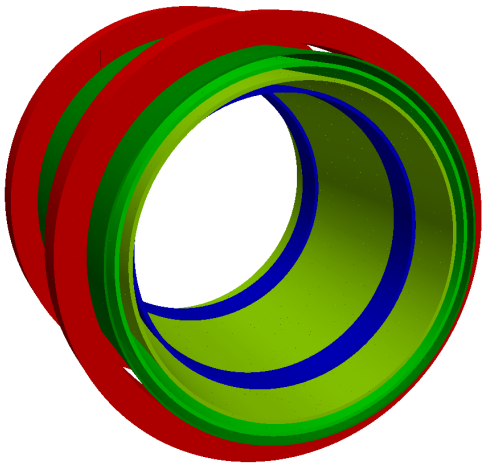

(b) 3D view

Figure 4: Test magnet problem with z (longitudinal) gradient coil: illustration of the components of the problem. (a) Axisymmetric meridian plane and (b) 3D view.

Off-line

Following the methodology described in Section 5.1.1, we apply Algorithm 1 and call OFFLINE $(\mathbf{A}(\boldsymbol{w}), \mathbf{R}(\boldsymbol{w}), \mathbf{W}_s, M)$ for the sets of samples $\mathbf{W}_s = (2\pi \mathrm{f}_1, 2\pi \mathrm{f}_2, \ldots, 2\pi \mathrm{f}_{N_s})$ with $N_s = 500, 250, 125, 63$, corresponding to $\mathrm{f}_i = 10 + (i-1)\Delta \mathrm{f}$ Hz, with $i = 1, \ldots, N_s$ and $\Delta \mathrm{f} = 10, 20, 40, 80$ Hz. The TSVD was truncated with $M = 50$ (leading to a maximum upper bound for the truncation error $e_1 = 8.3 \times 10^{-4}$ for the case $N_s = 500$). We use this offline data in the following subsections.

On-line PODI

In the case of PODI, Algorithm 2 is applied by calling ONLINEPODI$(\mathbf{H}^M, \mathbf{\Sigma}^M, \mathbf{G}^M, \mathbf{O}, M, \boldsymbol{x}, 2\pi \mathrm{f}_i)$ to compute $\boldsymbol{q}^{PODI}(\boldsymbol{x}, 2\pi \mathrm{f}_i)$ at the frequencies $\mathrm{f}_i = 15 + (i-1)\Delta \mathrm{f}$ Hz with $i = 1, \ldots, N_o$, $N_o = 499$ and $\Delta \mathrm{f} = 10$ Hz. Similarly, the full order solver is then used to compute $\boldsymbol{q}_{hpq}(\boldsymbol{x}, 2\pi \mathrm{f}_i)$ with f_i as before. This is then used to compute the dissipated power and kinetic energy, which, for the full order model, is defined as

$$P^0_\Omega(\boldsymbol{w}, \boldsymbol{\mathcal{A}}^{AC}_{\varepsilon,hq}(\boldsymbol{x}, \boldsymbol{w}), \boldsymbol{B}^{DC}_{0,hq}(\boldsymbol{x}), \boldsymbol{\mathcal{U}}^{AC}_{hp}(\boldsymbol{x}, \boldsymbol{w})) := \frac{1}{2} \int_\Omega \gamma \left| \boldsymbol{\mathcal{E}}^{AC}_{hpq} \right|^2 d\Omega$$

$$= \frac{1}{2} \int_\Omega \gamma \left| -\mathrm{i}\omega \boldsymbol{\mathcal{A}}^{AC}_{\varepsilon,hq} + \mathrm{i}\omega \boldsymbol{B}^{DC}_{0,hq} \times \boldsymbol{\mathcal{U}}^{AC}_{hp} \right|^2 d\Omega, \tag{31a}$$

$$E^k_\Omega(\boldsymbol{w}, \boldsymbol{\mathcal{U}}^{AC}_{hp}(\boldsymbol{x}, \boldsymbol{w})) := \frac{1}{2} \int_\Omega \rho \omega^2 \left| \boldsymbol{\mathcal{U}}^{AC}_{hp} \right|^2 d\Omega, \tag{31b}$$

where $\boldsymbol{B}^{DC}_{0,hq}$ is the finite element approximation to $\boldsymbol{B}^{DC}_0 = \operatorname{curl} \boldsymbol{A}^{DC}$ and $\boldsymbol{w} = \omega$ in the current case. The corresponding PODI approximations are $P^0_\Omega(\boldsymbol{w}, \boldsymbol{\mathcal{A}}^{PODI}(\boldsymbol{x}, \boldsymbol{w}), \boldsymbol{B}^{DC}_{0,hq}(\boldsymbol{x}), \boldsymbol{\mathcal{U}}^{PODI}(\boldsymbol{x}, \boldsymbol{w}))$ and $E^k_\Omega(\boldsymbol{w}, \boldsymbol{B}^{DC}_{0,hq}, \boldsymbol{\mathcal{U}}^{PODI}(\boldsymbol{x}, \boldsymbol{w}))$, which reduce to $P^0_\Omega(\omega, \boldsymbol{\mathcal{A}}^{PODI}, \boldsymbol{B}^{DC}_{0,hq}, \boldsymbol{\mathcal{U}}^{PODI})$ and $E^k_\Omega(\omega, \boldsymbol{B}^{DC}_{0,hq}, \boldsymbol{\mathcal{U}}^{PODI})$, respectively, where we have dropped the $(\boldsymbol{x}, \omega)$ dependency on the PODI solutions for simplicity of notation.

The outputs (31a) and (31b) can be computed for Ω_{4K}, Ω_{77K} or Ω_{OVC}. We choose to present the results for the worst performing of these, which, in the case of PODI, is Ω_{77K}. A comparison of $P^0_{\Omega_{77K}}(2\pi \mathrm{f}_i, \boldsymbol{\mathcal{A}}^{AC}_{\varepsilon,hq}, \boldsymbol{B}^{DC}_{0,hq}, \boldsymbol{\mathcal{U}}^{AC}_{hp})$ and $P^0_{\Omega_{77K}}(2\pi \mathrm{f}_i, \boldsymbol{\mathcal{A}}^{PODI}, \boldsymbol{B}^{DC}_{0,hq}, \boldsymbol{\mathcal{U}}^{PODI})$, $i = 1, \ldots, N_o$, is provided in Figure 5a. Similarly, $E^k_{\Omega_{77K}}(2\pi \mathrm{f}_i, \boldsymbol{\mathcal{U}}^{AC}_{hp})$ and $E^k_{\Omega_{77K}}(2\pi \mathrm{f}_i, \boldsymbol{\mathcal{U}}^{PODI})$, $i = 1, \ldots, N_o$, are compared in

Figure 5b. It can be observed how the resolution of the resonant peaks decreases with N_s, which leads, in the worst case, to the appearance of non-existent peaks or missing existent peaks. Note that these results correspond to the case where $I_j(\omega)$ is chosen to give a linear interpolation and no significant difference is observed in the case of Lagrange cubic interpolation. In this case there is no substantial improvement for Ω_{4K} or Ω_{OVC} and we refer to [38] for further details. In order to examine the loss in resolution more clearly we show, in Figure 6, a comparison between $E^k_{\Omega_{77K}}(2\pi \mathrm{f}_i, \boldsymbol{u}^{PODI})$, $3400 \leqslant \mathrm{f}_i \leqslant 5000$ Hz, for different N_s, and $E^k_{\Omega_{77K}}(2\pi \mathrm{f}_i, \boldsymbol{u}^{AC}_{hp})$ for different N_o (with f_i appropriately redefined). These results show that the N_s that PODI requires in order to accurately reproduce the dissipated power and kinetic energy in the radiation shields must be as large as the N_o required by the full order solver. Therefore, PODI does not offer advantages over a full order solution.

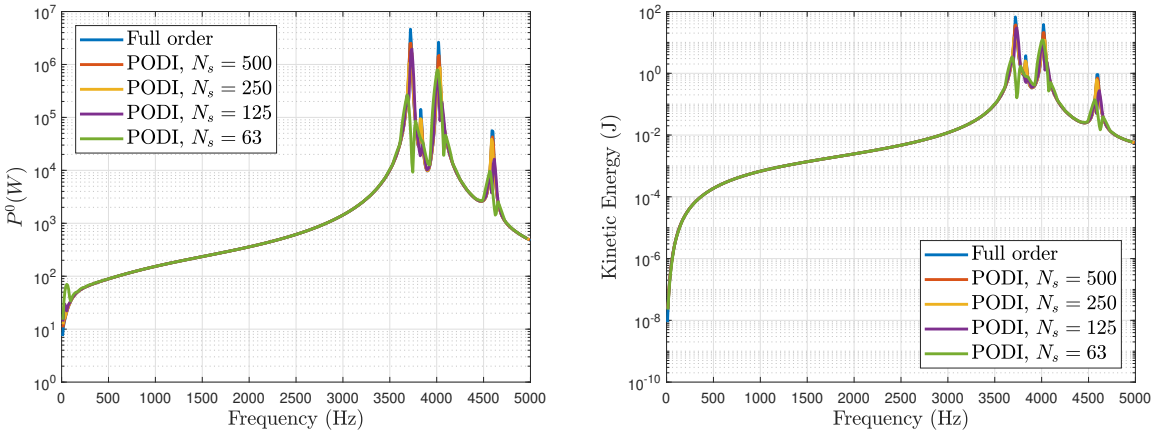

(a) $P^0_{\Omega_{77K}}$ (b) $E^k_{\Omega_{77K}}$

Figure 5: PODI applied to test magnet problem with 1 parameter: (a) Dissipated power and (b) kinetic energy in Ω_{77K}. Comparison with full order solution.

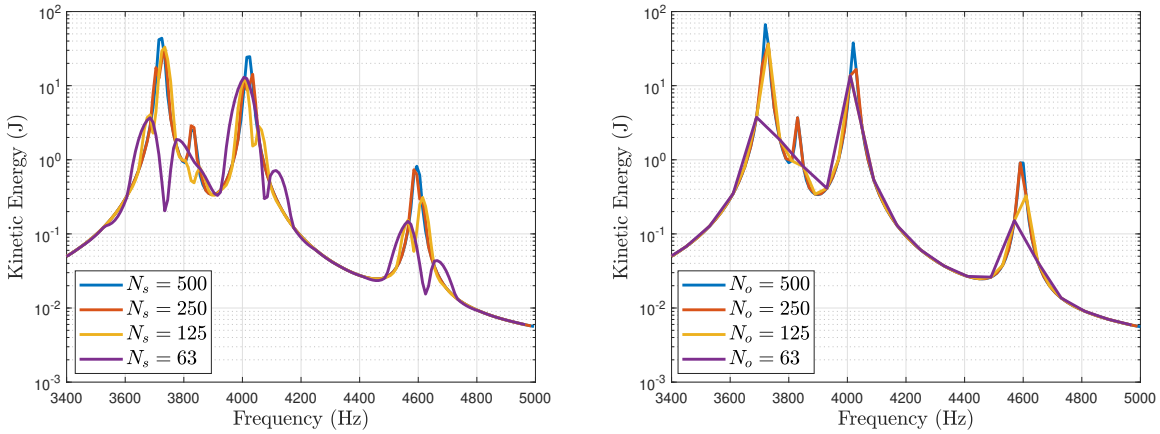

(a) $E^k_{\Omega_{77K}}(2\pi \mathrm{f}_i, \boldsymbol{u}^{PODI})$ (b) $E^k_{\Omega_{77K}}(2\pi \mathrm{f}_i, \boldsymbol{u}^{AC}_{hp})$

Figure 6: Test magnet problem with 1 parameter: (a)$E^k_{\Omega_{77K}}(2\pi \mathrm{f}_i, \boldsymbol{u}^{PODI})$ for different N_s and (b) $E^k_{\Omega_{77K}}(2\pi \mathrm{f}_i, \boldsymbol{u}^{AC}_{hp})$ for different N_o.

On-line PODP

In this Section we only wish to remark that there is no significant benefit in applying PODP instead of PODI to the complete problem (14) for the test magnet example. The results obtained by applying PODP

by calling ONLINEPODP($\mathbf{H}^M, \mathbf{A}^M(2\pi \mathrm{f}_i), \mathbf{R}^M(2\pi \mathrm{f}_i), \mathbf{O}, \boldsymbol{x}, 2\pi \mathrm{f}_i$) can be found in [38].

6.1.2 Application to Separated Physics Solutions

The purpose of this section is to investigate if there are benefits in applying PODI or PODP to the separated physics for the test magnet problem. This is motivated by the fact that $||\boldsymbol{\mathcal{A}}^{AC}_{\varepsilon,hq}||_{L^2(\Omega_{C,n})}$ has a smoother variation with frequency than $||\boldsymbol{\mathcal{U}}^{AC}_{hp}||_{L^2(\Omega_{C,n})}$ (where $\Omega_{C,n}$ refers to either Ω_{4K}, Ω_{77K} or Ω_{OVC}), as shown in Figure 3. Specifically, we now consider the application of PODI and PODP to the electromagnetic, $\boldsymbol{q}(\boldsymbol{x}, \omega) = \boldsymbol{\mathcal{A}}^{AC}_{\varepsilon}(\boldsymbol{x}, \omega)$, and mechanical, $\boldsymbol{q}(\boldsymbol{x}, \omega) = \boldsymbol{\mathcal{U}}^{AC}(\boldsymbol{x}, \omega)$, solutions separately, as explained in Section 5.2. The main goal of this study is to assess the efficiency of POD in approximating the electromagnetic and mechanical solutions, separately.

Off-line

At the *off-line* stage, we call first OFFLINE($\mathbf{A}_{\mathcal{A}\mathcal{A}}(\boldsymbol{w}), \mathbf{R}_{\mathcal{A}}(\boldsymbol{w}), \mathbf{W}_{\mathrm{s}}, M$) and then OFFLINE($\mathbf{A}_{\mathcal{U}\mathcal{U}}(\boldsymbol{w}), -\mathbf{A}_{\mathcal{U}\mathcal{A}}(\boldsymbol{w})\boldsymbol{\mathcal{A}}^{\mathrm{AC}}_{\varepsilon}(\boldsymbol{w}), \mathbf{W}_{\mathrm{s}}, M$) for $\mathbf{W}_s = (2\pi \mathrm{f}_1, 2\pi \mathrm{f}_2, \ldots, 2\pi \mathrm{f}_{N_s})$ with $f_i = 10 + (i-1)\Delta \mathrm{f}$, $i = 1, \ldots, N_s$, $N_s = 250, 63$ and $\Delta \mathrm{f} = 20, 80$ Hz. The TSVD was truncated after $M = 50$ in both cases, which leads to a maximum upper bound for the truncation error $e_1 = 1.1 \times 10^{-6}$ for the case $\boldsymbol{q}(\boldsymbol{x}, \omega) = \boldsymbol{\mathcal{A}}^{AC}_{\varepsilon}(\boldsymbol{x}, \omega)$ and $e_1 = 1.3 \times 10^{-4}$ for the case $\boldsymbol{q}(\boldsymbol{x}, \omega) = \boldsymbol{\mathcal{U}}^{AC}(\boldsymbol{x}, \omega)$, corresponding to $N_s = 250$. Note that e_1 is smaller in the case $\boldsymbol{q}(\boldsymbol{x}, \omega) = \boldsymbol{\mathcal{A}}^{AC}_{\varepsilon}(\boldsymbol{x}, \omega)$ than in the case $\boldsymbol{q}(\boldsymbol{x}, \omega) = \boldsymbol{\mathcal{U}}^{AC}(\boldsymbol{x}, \omega)$, which means that given a certain tolerance for e_1, fewer modes are needed to approximate $\boldsymbol{\mathcal{A}}^{AC}_{\varepsilon,hq}(\boldsymbol{x}, \omega)$ compared to $\boldsymbol{\mathcal{U}}^{AC}_{hp}(\boldsymbol{x}, \omega)$ (see [38] for further details). Note that $M = 50$ was chosen so that e_1 is sufficiently small for both physics.

On-line PODI

In the *on-line* stage, we call ONLINEPODI($\mathbf{H}^M_{\mathcal{A}}, \boldsymbol{\Sigma}^M_{\mathcal{A}}, \mathbf{G}^M_{\mathcal{A}}, \mathbf{N}, M, \boldsymbol{x}, 2\pi \mathrm{f}_i$) and then ONLINEPODI($\mathbf{H}^M_{\mathcal{U}}, \boldsymbol{\Sigma}^M_{\mathcal{U}}, \mathbf{G}^M_{\mathcal{U}}, \mathbf{L}, M, \boldsymbol{x}, 2\pi \mathrm{f}_i$), with f_i defined as in Section 6.1.1 i.e., unlike the extreme case in Section 6.1.1 where $N_o \approx N_s = 500$, we have now chosen $N_o = 499 > N_s$. The cases of $I_j(2\pi \mathrm{f}_i)$ corresponding to linear and cubic Lagrange interpolation were considered. The error $e_2(\mathbf{q}(2\pi \mathrm{f}_i), \mathbf{q}^{\mathrm{PODI}}(2\pi \mathrm{f}_i))$ is shown in Figure 7, where we can see that $e_2(\mathbf{q}(2\pi \mathrm{f}_i), \mathbf{q}^{\mathrm{PODI}}(2\pi \mathrm{f}_i))$ is several orders of magnitude smaller in the case $\mathbf{q}(2\pi \mathrm{f}_i) = \boldsymbol{\mathcal{A}}^{\mathrm{AC}}_{\varepsilon}(2\pi \mathrm{f}_i)$ compared to the case $\mathbf{q}(2\pi \mathrm{f}_i) = \boldsymbol{\mathcal{U}}^{\mathrm{AC}}(2\pi \mathrm{f}_i)$, especially for $\mathrm{f}_i > 3000$ Hz. The large $e_2(\mathbf{q}(2\pi \mathrm{f}_i), \mathbf{q}^{\mathrm{PODI}}(2\pi \mathrm{f}_i))$ obtained for the case $\mathbf{q}(2\pi \mathrm{f}_i) = \boldsymbol{\mathcal{A}}^{\mathrm{AC}}_{\varepsilon}(2\pi \mathrm{f}_i)$ at frequencies $\mathrm{f}_i < 1000$ Hz is due to its sharp variation in that region, and this can be predicted and taken into account when defining the sampling frequencies. However, the large $e_2(\mathbf{q}(2\pi \mathrm{f}_i), \mathbf{q}^{\mathrm{PODI}}(2\pi \mathrm{f}_i))$ obtained for $\mathbf{q}(2\pi \mathrm{f}_i) = \boldsymbol{\mathcal{U}}^{\mathrm{AC}}(2\pi \mathrm{f}_i)$ in the resonant region is due to the singularities (peaks) obtained when the electromagnetic field excites some of the resonant modes of the mechanical system, and cannot be predicted. Thus, the error $e_2(\mathbf{q}(2\pi \mathrm{f}_i), \mathbf{q}^{\mathrm{PODI}}(2\pi \mathrm{f}_i))$ in the resonant region is $O(1)$ for the case $\boldsymbol{q}(\boldsymbol{x}, \omega) = \boldsymbol{\mathcal{U}}^{AC}(\boldsymbol{x}, \omega)$ and the chosen N_s. To achieve a smaller e_2, N_s needs to be increased so that $N_s \approx N_o$ and, thus, there is no benefit gained from applying PODI to the mechanical problem. Furthermore, it can be observed that the error decreases as N_s increases and also that cubic interpolation offers a slightly improved accuracy compared to linear interpolation.

On-line PODP

The same conclusion holds also for the case of PODP, where only a marginal gain over PODI is obtained [38].

6.1.3 Combined Reduced Order–Full Order Approach

The purpose of this section is to study the accuracy and efficiency of the PODI-Full and PODP-Full methodologies presented in 5.3. This is motivated by the results in Section 6.1.2, where it was shown

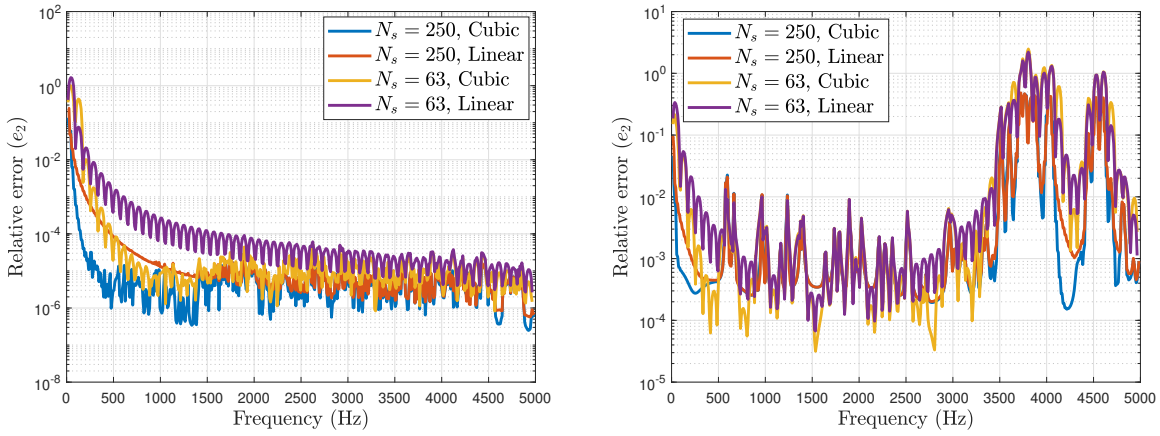

(a) $\mathbf{q}(2\pi \mathrm{f}_i) = \boldsymbol{\mathcal{A}}_{\varepsilon}^{\mathrm{AC}}(2\pi \mathrm{f}_i)$ (b) $\mathbf{q}(2\pi \mathrm{f}_i) = \boldsymbol{\mathcal{U}}^{\mathrm{AC}}(2\pi \mathrm{f}_i)$

Figure 7: PODI applied to test magnet problem with 1 parameter: relative error, $e_2(\mathbf{q}(2\pi \mathrm{f}_i), \mathbf{q}^{\mathrm{PODI}}(2\pi \mathrm{f}_i))$ for (a) $\mathbf{q}(2\pi \mathrm{f}_i) = \boldsymbol{\mathcal{A}}_{\varepsilon}^{\mathrm{AC}}(2\pi \mathrm{f}_i)$ and (b) $\mathbf{q}(2\pi \mathrm{f}_i) = \boldsymbol{\mathcal{U}}^{\mathrm{AC}}(2\pi \mathrm{f}_i)$.

for separated physics solutions, that the relative error $e_2(\mathbf{q}(\omega), \mathbf{q}^{\mathrm{POD}}(\omega))$ is several orders of magnitude smaller for the case $\mathbf{q}(\omega) = \boldsymbol{\mathcal{A}}_{\varepsilon}^{\mathrm{AC}}(\omega)$ than for the case $\mathbf{q}(\omega) = \boldsymbol{\mathcal{U}}^{\mathrm{AC}}(\omega)$.

Off-line

In Figure 7 it was observed that for the case of $\mathbf{q}(\omega) = \boldsymbol{\mathcal{A}}_{\varepsilon}^{\mathrm{AC}}(\omega)$, the error is higher for $f < 1000$ Hz. Therefore, a non uniform Δf will be used. In particular, the sampling frequencies are defined as:

$$\mathrm{f}_i = \begin{cases} 10 \text{ Hz} & \text{if} \quad i = 1 \\ 10 + (i-1)\Delta \mathrm{f}_1 \text{ Hz} & \text{if} \quad \mathrm{f}_{i-1} < 1000 \text{ Hz and } i > 1 \\ 10 + (i-1)\Delta \mathrm{f}_2 \text{ Hz} & \text{if} \quad \mathrm{f}_{i-1} \geqslant 1000 \text{ Hz and } i > 1 \end{cases}, \tag{32}$$

with $i = 1, \ldots, N_s$. The frequency steps $(\Delta \mathrm{f}_1, \Delta \mathrm{f}_2) = \{(10, 50), (20, 100), (40, 200), (80, 400)\}$ Hz where considered, which results in a set of samples $\mathbf{W}_{\mathrm{s}} = \{2\pi \mathrm{f}_1, 2\pi \mathrm{f}_2, \ldots, 2\pi \mathrm{f}_{N_s}\}$ with $N_s = 180, 90, 45$ and 23, respectively. We apply Algorithm 1 and call OFFLINE$(\mathbf{A}_{\mathcal{A}\mathcal{A}}(\boldsymbol{w}), \mathbf{R}_{\mathcal{A}}(\boldsymbol{w}), \mathbf{W}_{\mathrm{s}}, M)$ with $M = 20$ (leading to a maximum upper bound for the truncation error $e_1 = 8.9 \times 10^{-6}$ for the case $N_s = 180$).

On-line PODI-Full

In this stage, Algorithm 4 is applied by calling ONLINEPODI-FULL$(\mathbf{H}_{\mathcal{A}}^{M}, \boldsymbol{\Sigma}_{\mathcal{A}}^{M}, \mathbf{G}_{\mathcal{A}}^{M}, \mathbf{A}_{\mathcal{U}\mathcal{U}}(2\pi \mathrm{f}_i), \mathbf{A}_{\mathcal{U}\mathcal{A}}(2\pi \mathrm{f}_i), \mathbf{N}, \mathbf{L}, M, \boldsymbol{x}, 2\pi \mathrm{f}_i)$ with $\mathrm{f}_i = 15 + (i-1)\Delta \mathrm{f}$, $i = 1, \ldots, N_o$, $N_o = 499 > N_s$ and $\Delta \mathrm{f} = 10$ Hz. A comparison of $P^0_{\Omega_{C,n}}(2\pi \mathrm{f}_i, \boldsymbol{\mathcal{A}}^{PODI-FULL}, \boldsymbol{B}^{DC}_{0,hq}, \boldsymbol{\mathcal{U}}^{PODI-FULL})$ with $P^0_{\Omega_{C,n}}(2\pi \mathrm{f}_i, \boldsymbol{\mathcal{A}}^{AC}_{\varepsilon,hq}, \boldsymbol{B}^{DC}_{0,hq}, \boldsymbol{\mathcal{U}}^{AC}_{hp})$ and $E^k_{\Omega_{C,n}}(2\pi \mathrm{f}_i, \boldsymbol{\mathcal{U}}^{PODI-FULL})$ with $E^k_{\Omega_{C,n}}(2\pi \mathrm{f}_i, \boldsymbol{\mathcal{U}}^{AC}_{hp})$, where $\Omega_{C,n}$ refers to either Ω_{4K}, Ω_{77K} or Ω_{OVC}, is shown in Figure 8, with $i = 1, \ldots, N_o$ in all cases. It can be observed that the results show an excellent agreement with the full order solution and differences are only observed at $f < 200$ Hz for $P^0_{\Omega_{4K}}$ and $P^0_{\Omega_{77K}}$ in the case $N_s = 23$.

To further study the accuracy of the method, the relative error $e_2(\boldsymbol{\mathcal{A}}_{\varepsilon}^{\mathrm{AC}}(2\pi \mathrm{f}_i), \boldsymbol{\mathcal{A}}^{\text{PODI-FULL}}(2\pi \mathrm{f}_i))$ and $e_2(\boldsymbol{\mathcal{U}}^{\mathrm{AC}}(2\pi \mathrm{f}_i), \boldsymbol{\mathcal{U}}^{\text{PODI-FULL}}(2\pi \mathrm{f}_i))$ are shown in Figures 9a and 9b, respectively.

These results show that $\boldsymbol{\mathcal{A}}^{\mathrm{PODI-FULL}}$ produced by Algorithm 4 is able to accurately reproduce $\boldsymbol{\mathcal{A}}^{AC}_{\varepsilon,hq}$ already by using a small N_s. The method is much more robust than the application of PODI to the whole problem, as the peaks are very accurately resolved even for only $N_s = 23$ and the error $e_2(\boldsymbol{\mathcal{U}}^{\mathrm{AC}}(2\pi \mathrm{f}_i), \boldsymbol{\mathcal{U}}^{\text{PODI-FULL}}(2\pi \mathrm{f}_i))$ in the resonant region ($\mathrm{f}_i > 3000$ Hz) is around three orders of magnitude smaller than when applying PODI to the complete problem. Furthermore, the method offers a

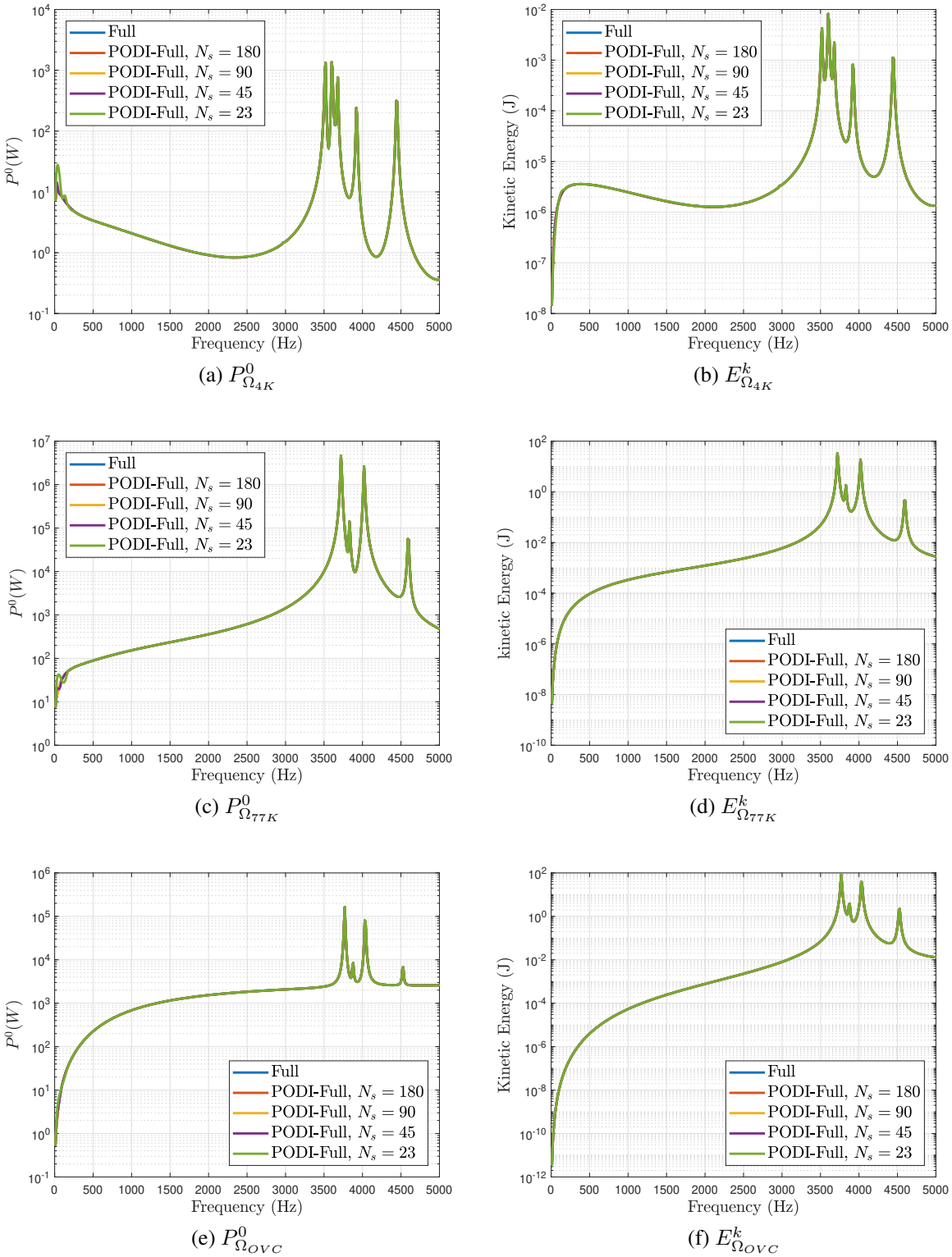

(a) $P^0_{\Omega_{4K}}$ (b) $E^k_{\Omega_{4K}}$

(c) $P^0_{\Omega_{77K}}$ (d) $E^k_{\Omega_{77K}}$

(e) $P^0_{\Omega_{OVC}}$ (f) $E^k_{\Omega_{OVC}}$

Figure 8: PODI-Full applied to test magnet problem with 1 parameter: (a) $P^0_{\Omega_{4K}}$, (b) $E^k_{\Omega_{4K}}$, (c) $P^0_{\Omega_{77K}}$, (d) $E^k_{\Omega_{77K}}$, (e) $P^0_{\Omega_{OVC}}$ and (f) $E^k_{\Omega_{OVC}}$. Comparison with full order solution.

great advantage in terms of computational speed. To illustrate this, a comparison of solver time between PODI-Full and the full order solver is provided in Figure 10a, where the cases of $N_s = 23, 45$ and $N_o = 125, 250, 500, 1000$ have been considered. For the full order solver, the total time is shown (including assembly and solution of the linear systems), while for PODI-Full both the off-line (including

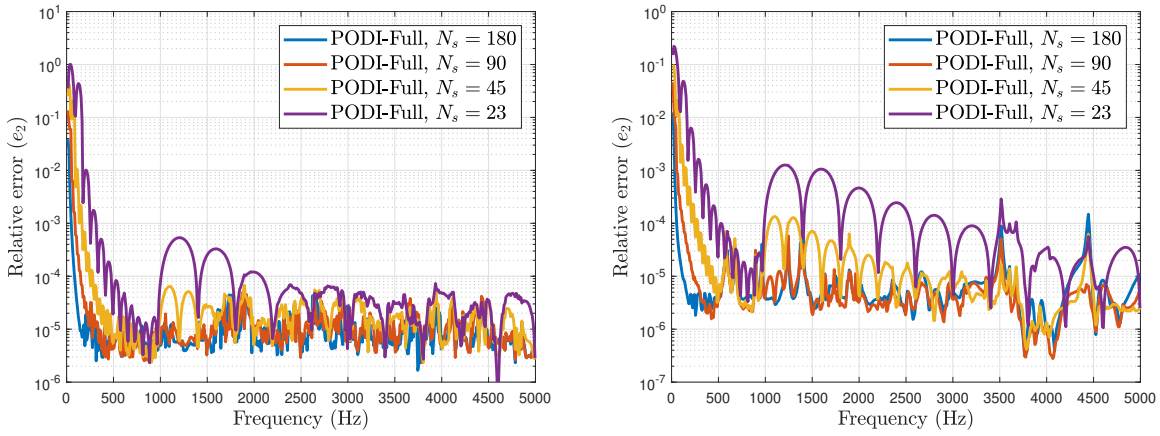

(a) $e_2(\boldsymbol{\mathcal{A}}_{\varepsilon}^{\text{AC}}(2\pi \text{f}_i), \boldsymbol{\mathcal{A}}^{\text{PODI-FULL}}(2\pi \text{f}_i))$ (b) $e_2(\boldsymbol{\mathcal{U}}^{\text{AC}}(2\pi \text{f}_i), \boldsymbol{\mathcal{U}}^{\text{PODI-FULL}}(2\pi \text{f}_i))$

Figure 9: PODI-Full applied to test magnet problem with 1 parameter: (a) $e_2(\boldsymbol{\mathcal{A}}_{\varepsilon}^{\text{AC}}(2\pi \text{f}_i), \boldsymbol{\mathcal{A}}^{\text{PODI-FULL}}(2\pi \text{f}_i))$ and (b) $e_2(\boldsymbol{\mathcal{U}}^{\text{AC}}(2\pi \text{f}_i), \boldsymbol{\mathcal{U}}^{\text{PODI-FULL}}(2\pi \text{f}_i))$.

assembly) and total times are shown. Figure 10b shows the speed-up with respect to the full order solver. Note for example the case $N_s = 45$ (where there is no appreciable difference in the solution), where the speed up is 45 % for $N_o = 125$ and grows to 84 % for $N_o = 1000$. The solver time is clock time and all the computations reported in this work were made in a cluster node using a machine *Bull Sequana X440-E5 2 x Octa-Core (3.2 GHz) Xeon Gold v5 6134* and using a parallel pool of 8 workers to solve the frequency sweeps in parallel. Unless otherwise stated all the computational time measurements in this document are based on these settings.

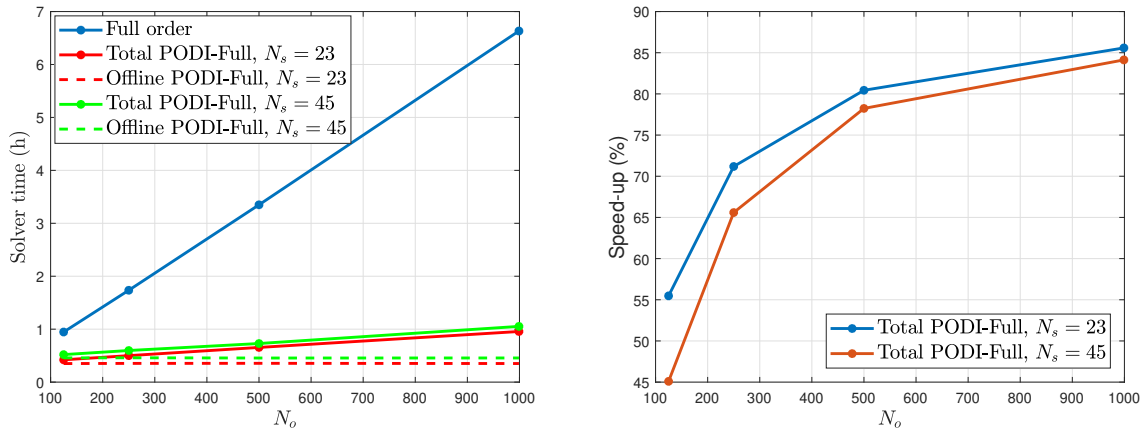

(a) Solver Time (b) Speed-up

Figure 10: PODI-Full applied to test magnet problem with 1 parameter: (a) Solver time and (b) speed-up for different values of N_s and N_o.

On-line PODP-Full

In this Section, the study presented above for PODI-Full is now repeated for the PODP-Full approach, by applying Algorithm 5 and calling ONLINEPODP-FULL($\mathbf{H}_{\mathcal{A}}^{M}, \mathbf{A}(2\pi \text{f}_i), \mathbf{R}(2\pi \text{f}_i), \mathbf{N}, \mathbf{L}, \boldsymbol{x}, 2\pi \text{f}_i$), with $\text{f}_i = 15 + (i-1)\Delta\text{f}$, $i = 1, \ldots, N_o$, $N_o = 499 > N_s$ and $\Delta\text{f} = 10$ Hz. A comparison of $P^0_{\Omega_{C,n}}(2\pi \text{f}_i, \boldsymbol{\mathcal{A}}^{PODP-FULL}, \boldsymbol{B}^{DC}_{0,hq}, \boldsymbol{\mathcal{U}}^{PODP-FULL})$ with $P^0_{\Omega_{C,n}}(2\pi \text{f}_i, \boldsymbol{\mathcal{A}}^{AC}_{\varepsilon,hq}, \boldsymbol{B}^{DC}_{0,hq}, \boldsymbol{\mathcal{U}}^{AC}_{hp})$ and

$E^k_{\Omega_{C,n}}(2\pi \mathrm{f}_i, \boldsymbol{u}^{PODP-FULL})$ with $E^k_{\Omega_{C,n}}(2\pi \mathrm{f}_i, \boldsymbol{u}^{AC}_{hp})$, where $\Omega_{C,n}$ refers to either Ω_{4K}, Ω_{77K} or Ω_{OVC}, is shown in Figure 11, with $i = 1, \ldots, N_o$ in all cases. It can be observed that the results obtained by applying Algorithm 5 are in excellent agreement with the full order results. With this approach there is no visible difference with the full order results even for $N_s = 23$.

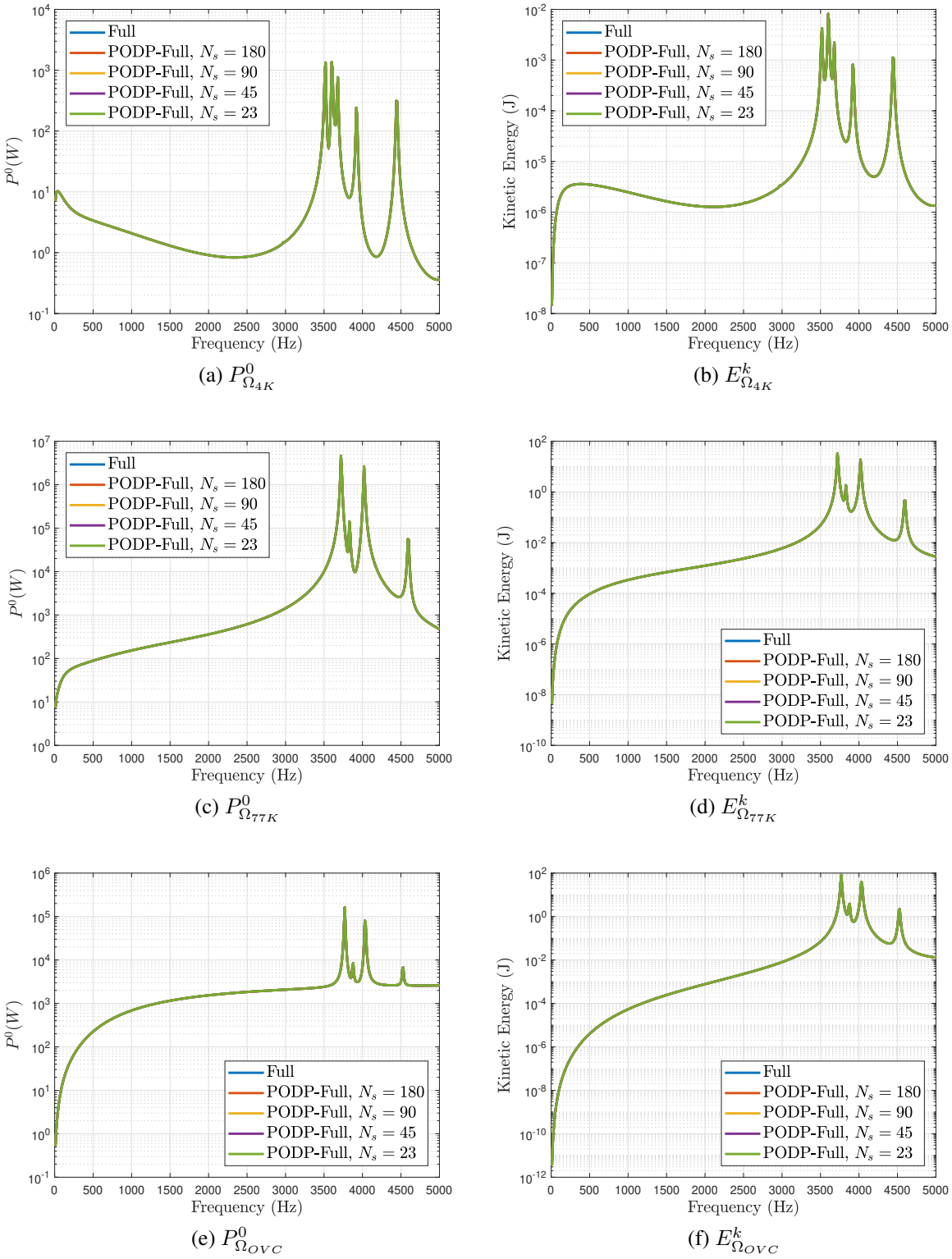

(a) $P^0_{\Omega_{4K}}$ (b) $E^k_{\Omega_{4K}}$

(c) $P^0_{\Omega_{77K}}$ (d) $E^k_{\Omega_{77K}}$

(e) $P^0_{\Omega_{OVC}}$ (f) $E^k_{\Omega_{OVC}}$

Figure 11: PODP-Full applied to test magnet problem with 1 parameter: (a) $P^0_{\Omega_{4K}}$, (b) $E^k_{\Omega_{4K}}$, (c) $P^0_{\Omega_{77K}}$, (d) $E^k_{\Omega_{77K}}$, (e) $P^0_{\Omega_{OVC}}$ and (f) $E^k_{\Omega_{OVC}}$. Comparison with full order solution.

Furthermore, in Figure 12, a comparison of solver time between PODP-Full and the full order solver is shown. Similarly to the results for PODI-Full (Figure 10), it can be observed that a speed-up higher than 85 % can be obtained. Similarly as before, the total time is shown for the full order case, while both the total and off-line times are shown for the PODP-Full approach. Note also that the speed-up obtained with Algorithm 4 and Algorithm 5 is almost identical, while a higher accuracy is obtained with Algorithm 5.

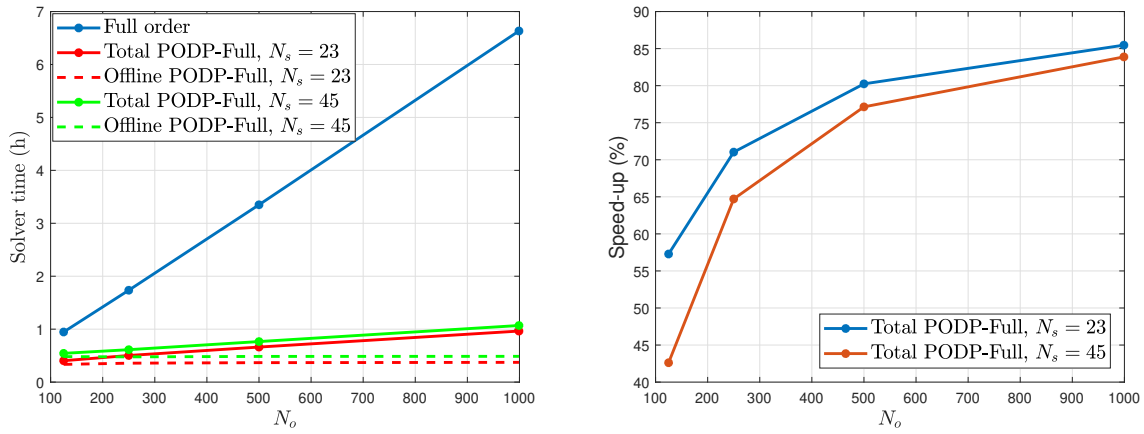

(a) Solver Time

(b) Speed-up

Figure 12: PODP-Full applied to test magnet problem with 1 parameter: (a) Solver time and (b) speed-up for different values of N_s and N_o.

6.2 Test Magnet Problem with Multiple Parameters

We now reconsider the problem described in Section 6.1 with both the frequency and the conductivity of the OVC, γ^{OVC}, considered as parameters, this is, $\boldsymbol{w} = \left(\omega, \gamma^{OVC}\right)$. The conductivity γ^{OVC} is assumed to vary in the range $0.1\gamma_{ref}^{OVC} \leqslant \gamma^{OVC} \leqslant 10\gamma_{ref}^{OVC}$, being γ_{ref}^{OVC} the reference value used for the test magnet problem. Since in Section 6.1.3 we have seen that PODP-Full offers an increased accuracy compared with PODI-Full for almost no increase in computational cost, only PODP-Full will be considered in this multi-parameter case. Nevertheless, it should be noted that these differences might not be so significant if more advanced interpolation techniques are used.

Off-line

The number of sampled conductivities was set to $N_{\gamma_s} = 3$ and, for each of this conductivities, the number of sampled frequencies is set to $N_{\omega_s} = 45$, which results in a total number of samples $N_s = 135$. This means that $\mathbf{W}_\mathrm{s}$ has the elements $\mathbf{w}_k = (2\pi \mathrm{f}_i, \gamma_j^{OVC})$, $k = i + (j-1)N_{\omega_s}$, $i = 1, \ldots, N_{\omega_s}$, $j = 1, \ldots, N_{\gamma_s}$ where f_i is defined by (32) with $(\Delta \mathrm{f}_1, \Delta \mathrm{f}_2) = (40, 200)$ Hz and $\gamma_j^{OVC} = 0.1(10^{j-1})\gamma_{ref}^{OVC}$. We then apply Algorithm 1 and call OFFLINE$(\mathbf{A}_{\mathcal{A}\mathcal{A}}(\boldsymbol{w}), \mathbf{R}_{\mathcal{A}}(\boldsymbol{w}), \mathbf{W}_\mathrm{s}, M)$ where the TSVD was truncated with $M = 20$ (leading to an upper bound for the truncation error $e_1 = 1.6 \times 10^{-3}$).

On-line PODP-Full

The purpose of this section is the application of Algorithm 5 to a multiple parameter case of the test magnet problem. We achieve this by calling ONLINEPODP-FULL$(\mathbf{H}_{\mathcal{A}}^M, \mathbf{A}(\mathbf{w}_k), \mathbf{R}(\mathbf{w}_k), \mathbf{N}, \mathbf{L}, \boldsymbol{x}, \mathbf{w}_k)$ where $\mathbf{w}_k = (2\pi \mathrm{f}_i, \gamma_j^{OVC})$, $k = i + (j-1)N_{\omega_o}$, $i = 1, \ldots, N_{\omega_o}$, $j = 1, \ldots, N_{\gamma_o}$, $\mathrm{f}_i = 10 + \Delta \mathrm{f}(i - 1)$ Hz, $N_{\omega_o} = 500$, $\gamma_j^{OVC} \in (0.35, 0.75, 3.5, 7.5)\gamma_{ref}^{OVC}$, $N_{\gamma_o} = 4$ and $\Delta \mathrm{f} = 10$ Hz. A comparison of $P^0_{\Omega_{OVC}}(\mathbf{w}_k, \boldsymbol{\mathcal{A}}^{PODP-FULL}, \boldsymbol{B}^{DC}_{0,hq}, \boldsymbol{u}^{PODP-FULL})$ with $P^0_{\Omega_{OVC}}(\mathbf{w}_k, \boldsymbol{\mathcal{A}}^{AC}_{\varepsilon,hq}, \boldsymbol{B}^{DC}_{0,hq}, \boldsymbol{u}^{AC}_{hp})$ is shown in Figure 13a. Similarly a comparison of $E^k_{\Omega_{OVC}}(\mathbf{w}_k, \boldsymbol{u}^{PODP-FULL})$ with $E^k_{\Omega_{OVC}}(\mathbf{w}_k, \boldsymbol{u}^{AC}_{hp})$ is shown

in Figure 13b. It can be observed that the PODP-Full result is in perfect agreement with the full order solution. Excellent agreement is also observed in Ω_{4K} and Ω_{77K} [38].

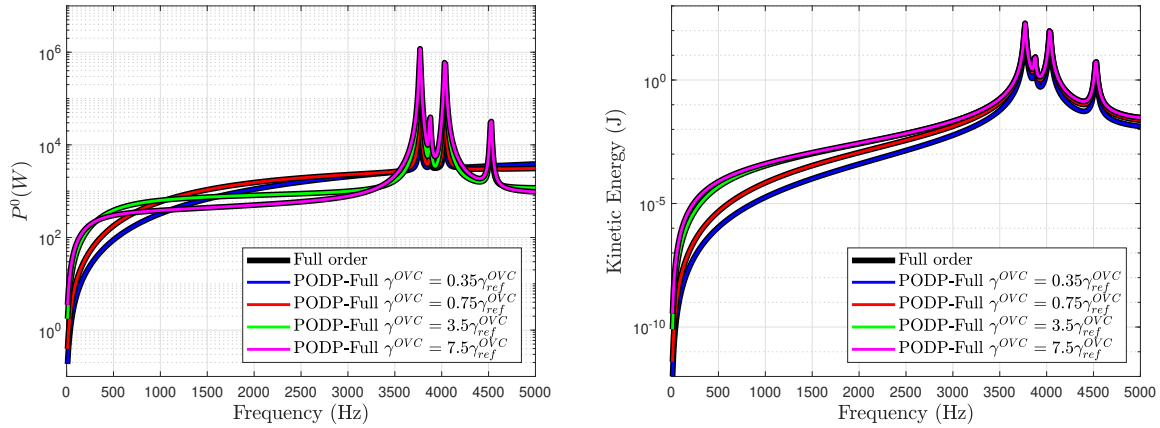

(a) $P^0_{\Omega_{OVC}}$ (b) $E^k_{\Omega_{OVC}}$

Figure 13: PODP-Full applied to test magnet problem with multiple parameters: (a) $P^0_{\Omega_{OVC}}$ and (b) $E^k_{\Omega_{OVC}}$ for different values of γ^{OVC}. Comparison with full order solution.

Next, in order to better benchmark the accuracy of the method, $e_2(\boldsymbol{\mathcal{A}}^{\text{AC}}_{\varepsilon}(\mathbf{w}_k), \boldsymbol{\mathcal{A}}^{\text{PODP-FULL}}(\mathbf{w}_k))$ and $e_2(\boldsymbol{\mathcal{U}}^{\text{AC}}(\mathbf{w}_k), \boldsymbol{\mathcal{U}}^{\text{PODP-FULL}}(\mathbf{w}_k))$ are computed, and the result is shown in Figure 14. The maximum $e_2(\boldsymbol{\mathcal{A}}^{\text{AC}}_{\varepsilon}(\mathbf{w}_k), \boldsymbol{\mathcal{A}}^{\text{PODP-FULL}}(\mathbf{w}_k))$ is 13 % for $f < 50$ Hz and is below 8 % for $f > 50$ Hz. Note that $e_2(\boldsymbol{\mathcal{U}}^{\text{AC}}(\mathbf{w}_k), \boldsymbol{\mathcal{U}}^{\text{PODP-FULL}}(\mathbf{w}_k))$ is smaller than $e_2(\boldsymbol{\mathcal{A}}^{\text{AC}}_{\varepsilon}(\mathbf{w}_k), \boldsymbol{\mathcal{A}}^{\text{PODP-FULL}}(\mathbf{w}_k))$, and that even though $e_2(\boldsymbol{\mathcal{A}}^{\text{AC}}_{\varepsilon}(\mathbf{w}_k), \boldsymbol{\mathcal{A}}^{\text{PODP-FULL}}(\mathbf{w}_k))$ is smaller at $f > 1000$ Hz, this is not true for the case $e_2(\boldsymbol{\mathcal{U}}^{\text{AC}}(\mathbf{w}_k), \boldsymbol{\mathcal{U}}^{\text{PODP-FULL}}(\mathbf{w}_k))$ due to the effect of the peaks in the resonant region. Furthermore, the accuracy can be improved if desired by increasing N_s (see [38]).

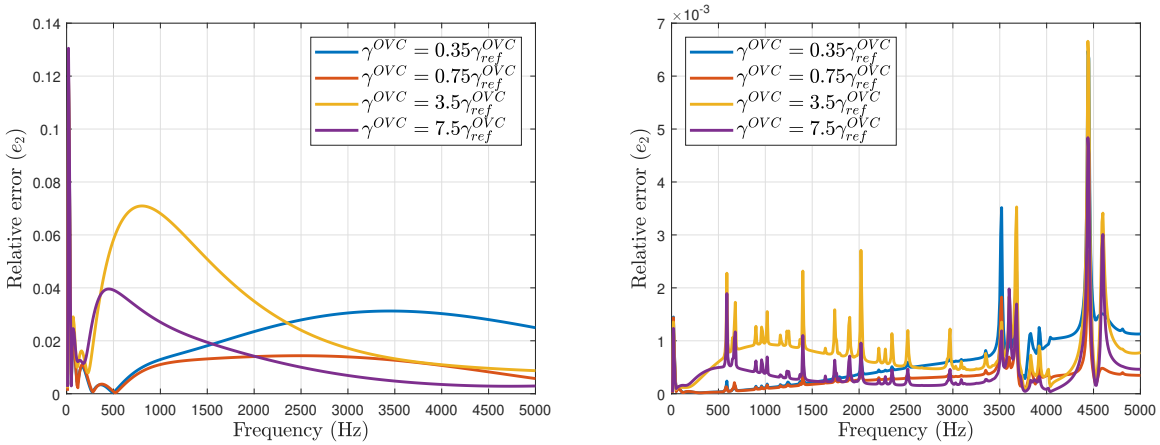

(a) $e_2(\boldsymbol{\mathcal{A}}^{\text{AC}}_{\varepsilon}(\mathbf{w}_k), \boldsymbol{\mathcal{A}}^{\text{PODP-FULL}}(\mathbf{w}_k))$ (b) $e_2(\boldsymbol{\mathcal{U}}^{\text{AC}}(\mathbf{w}_k), \boldsymbol{\mathcal{U}}^{\text{PODP-FULL}}(\mathbf{w}_k))$

Figure 14: PODP-Full applied to test magnet problem with multiple parameters: (a) $e_2(\boldsymbol{\mathcal{A}}^{\text{AC}}_{\varepsilon}(\mathbf{w}_k), \boldsymbol{\mathcal{A}}^{\text{PODP-FULL}}(\mathbf{w}_k))$ and (b) $e_2(\boldsymbol{\mathcal{U}}^{\text{AC}}(\mathbf{w}_k), \boldsymbol{\mathcal{U}}^{\text{PODP-FULL}}(\mathbf{w}_k))$.

The computational speed-up obtained with this method is also assessed comparing the time taken by the full order solver for different $N_o = N_{\gamma_o} N_{\omega_o}$ with the time taken by PODP-Full for different N_o and $N_s = 135$, with$\mathbf{w}_k$, $k = 1, \ldots N_o$, appropriately redefined. The result is shown in Figure 15, where for the full order case the total time is shown, which includes the assembly and the solution to the linear systems, while in the case of PODP-Full the total and off-line times are shown. It can be observed that

a massive speed-up of up to 90 % can be obtained[9]. As an example, consider the case $N_{\omega_o} = 500$ and $N_{\gamma_o} = 10$, this is, we want to compute a frequency sweep using a step $\Delta f = 10$ Hz for 10 different conductivities. The time required by the full order solver would be 31.8 h, while using the ROM, this reduces to only 3.8 h and of course the time saving increases as either N_{γ_o} or N_{ω_o} increase.

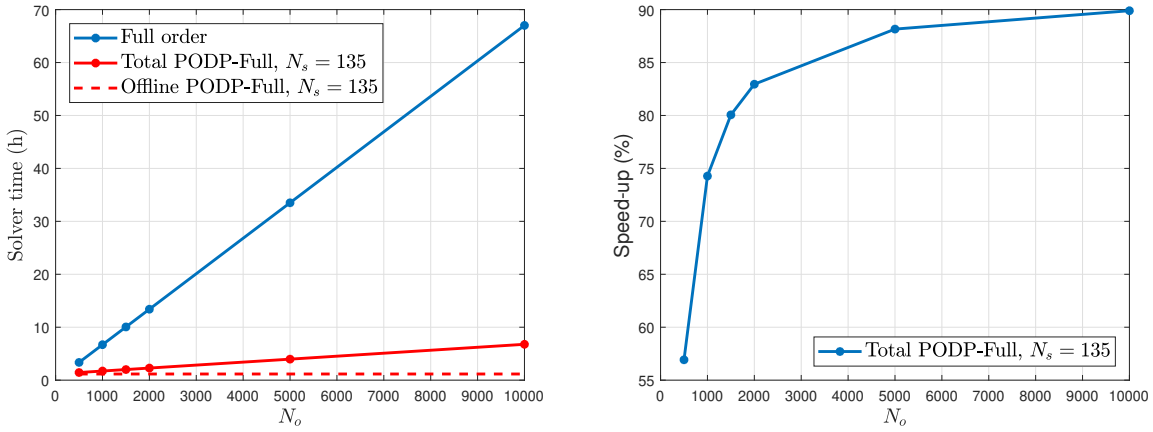

(a) Solver Time

(b) Speed-up

Figure 15: PODP-Full applied to test magnet problem with multiple parameters: (a) Solver time and (b) speed-up for different values of N_s and N_o.

Furthermore, in order to further assess the accuracy of the ROM, in Figure 16 we plot contours of the eddy currents $\boldsymbol{\jmath}^o_{hpq}(\boldsymbol{x}, \mathbf{w}) = \gamma \boldsymbol{\mathcal{E}}^{\mathrm{AC}}_{hpq}(\boldsymbol{x}, \mathbf{w}) = \gamma(-\mathrm{i}\omega \boldsymbol{\mathcal{A}}^{AC}_{\varepsilon,hq}(\boldsymbol{x}, \mathbf{w}) + \mathrm{i}\omega \boldsymbol{B}^{DC}_{0,hq} \times \boldsymbol{\mathcal{U}}^{AC}_{hp}(\boldsymbol{x}, \mathbf{w}))$ and its approximation $\boldsymbol{\jmath}^{PODP-FULL}(\boldsymbol{x}, \mathbf{w})$ in the deformed 77K shield for the case where $\mathbf{w} = (2000\pi, 0.35\gamma^{OVC}_{ref})$. It can be observed that an excellent agreement is obtained. Furthermore, a contour plot of $|\mathrm{Re}(\boldsymbol{\mathcal{U}}^{\mathrm{AC}}_{hp}(\boldsymbol{x}, \mathbf{w}))|$ and $|\mathrm{Re}(\boldsymbol{\mathcal{U}}^{PODP-FULL}(\boldsymbol{x}, \mathbf{w}))|$ in the 4K shield for the same parameters is shown in Figure 17, where again an excellent agreement is observed.

6.3 Modified Magnet Problem with Multiple Parameters

The application of the combined reduced order-full order methodology to a different problem is now considered. As opposed to the test magnet problem, each conducting shield has, in this new configuration, a different length. Furthermore, a transversal x gradient coil is now considered instead of the longitudinal z gradient coil. An illustration of the new configuration is provided in Figure 18. For further details about the geometry and boundary conditions we refer to [38]. A mesh of 54 796 elements and polynomial orders $p = 3$ and $q = 4$ were considered for the FE discretisation.
In this case, the frequency and the conductivity of the 77K shield, γ^{77K}, are considered as parameters, this is, $\boldsymbol{w} = (\omega, \gamma^{77K})$. The conductivity γ^{77K} is assumed to vary in the range $0.4\gamma^{77K}_{ref} \leqslant \gamma^{77K} \leqslant 2.5\gamma^{77K}_{ref}$, being γ^{77K}_{ref} the reference value used for the test magnet problem.

Off-line

The number of sampled conductivities was set to $N_{\gamma_s} = 3$ and, for each conductivity, the number of sampled frequencies is set to $N_{\omega_s} = 45$, which results in a total number of samples $N_s = 135$. This means that $\mathbf{W}_\mathrm{s}$ has the elements $\mathbf{w}_k = (2\pi \mathrm{f}_i, \gamma^{77K}_j)$, $k = i + (j-1)N_{\omega_s}$, $i = 1, \ldots, N_{\omega_s}$, $j = 1, \ldots, N_{\gamma_s}$ where f_i is defined by (32) with $(\Delta \mathrm{f}_1, \Delta \mathrm{f}_2) = (40, 200)$ Hz and $\gamma^{77K}_j \in (0.4, 1, 2.5)\gamma^{77K}_{ref}$. We then apply Algorithm 1 and call OFFLINE$(\mathbf{A}_{\mathcal{A}\mathcal{A}}(\boldsymbol{w}), \mathbf{R}_{\mathcal{A}}(\boldsymbol{w}), \mathbf{W}_\mathrm{s}, M)$ where the TSVD was truncated with $M = 20$ (leading to an upper bound for the truncation error $e_1 = 6.8 \times 10^{-3}$).

[9]Note that in the case of computational time for the full order solver only the first 4 points were measured, and

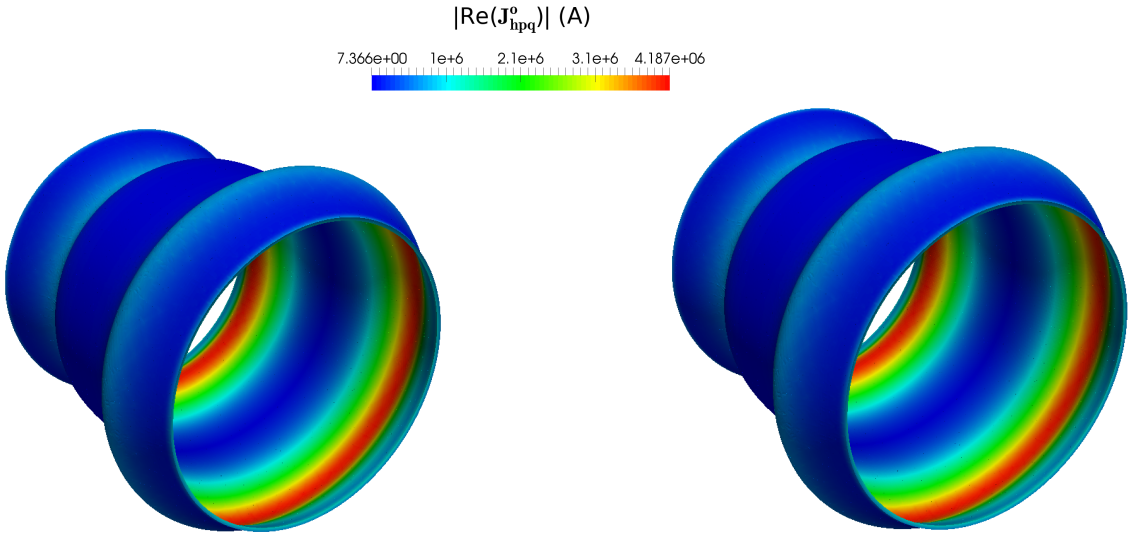

(a) $|\mathrm{Re}(\boldsymbol{\jmath}^o_{hpq}(\boldsymbol{x},\mathbf{w}))|$ (b) $|\mathrm{Re}(\boldsymbol{\jmath}^{PODP-FULL}(\boldsymbol{x},\mathbf{w}))|$

Figure 16: PODP-Full applied to test magnet problem with multiple parameters: Contours of (a) $|\mathrm{Re}(\boldsymbol{\jmath}^o_{hpq}(\boldsymbol{x},\mathbf{w}))|$ and (b) $|\mathrm{Re}(\boldsymbol{\jmath}^{PODP-FULL}(\boldsymbol{x},\mathbf{w}))|$ in the 77K shield for $\mathbf{w} = (2000\pi, 0.35\gamma^{OVC}_{ref})$ compared with the full order solution. Deformation exaggerated by a factor of 10^4.

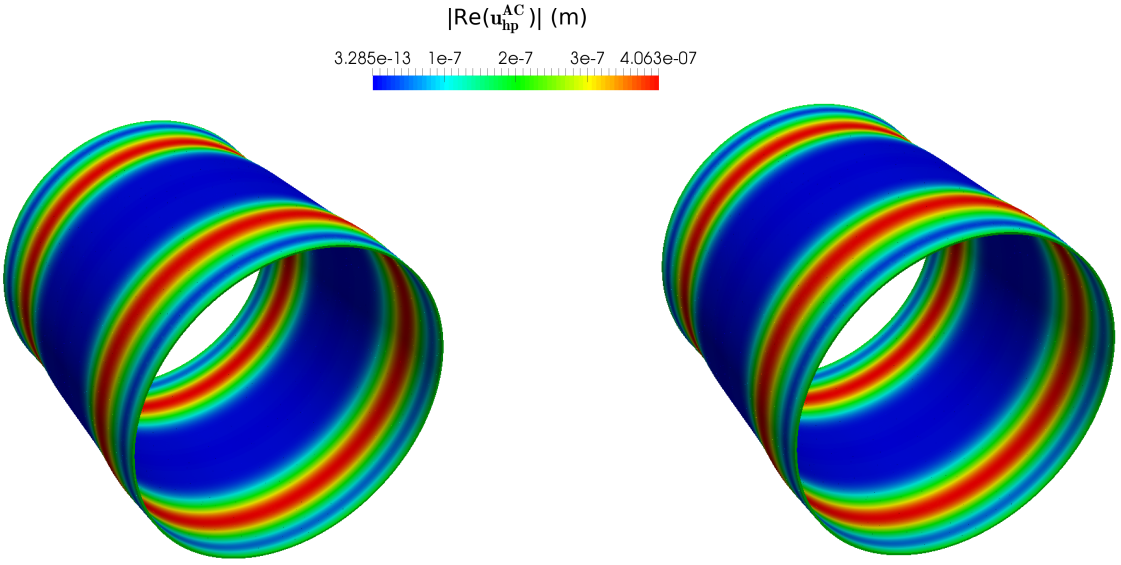

(a) $|\mathrm{Re}(\boldsymbol{u}^{\mathrm{AC}}_{hp}(\boldsymbol{x},\mathbf{w}))|$ (b) $|\mathrm{Re}(\boldsymbol{u}^{PODP-FULL}(\boldsymbol{x},\mathbf{w}))|$

Figure 17: PODP-Full applied to test magnet problem with multiple parameters: Contours of (a) $|\mathrm{Re}(\boldsymbol{u}^{\mathrm{AC}}_{hp}(\boldsymbol{x},\mathbf{w}))|$ and (b) $|\mathrm{Re}(\boldsymbol{u}^{PODP-FULL}(\boldsymbol{x},\mathbf{w}))|$ in the 4K shield for $\mathbf{w} = (2000\pi, 0.35\gamma^{OVC}_{ref})$. Deformation exaggerated by a factor of 10^4 in plot, but not in contours.

On-line PODP-Full

The purpose of this section is the application of Algorithm 5 to a multiple parameter case of the modified magnet problem. We achieve this by calling ONLINEPODP-FULL($\mathbf{H}^M_{\mathcal{A}}, \mathbf{A}(\mathbf{w}_k), \mathbf{R}(\mathbf{w}_k), \mathbf{N}, \mathbf{L}, \boldsymbol{x}, \mathbf{w}_k$) where $\mathbf{w}_k = (2\pi \mathrm{f}_i, \gamma^{77K}_j)$, $k = i + (j-1)N_{\omega_o}$, $i = 1,\ldots,N_{\omega_o}$, $j = 1,\ldots,N_{\gamma_o}$, $\mathrm{f}_i = 10 + \Delta\mathrm{f}(i-1)$,

the last two were extrapolated.

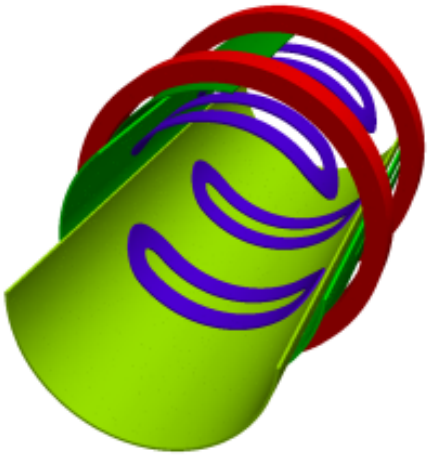

Figure 18: Modified magnet problem with x (transversal) gradient coil: illustration of the components of the problem.

Δf $= 10$ Hz, $N_{\omega_o} = 500$, $\gamma_j^{77K} \in (0.5, 0.75, 1.5, 2)\,\gamma_{ref}^{77K}$ and $N_{\gamma_o} = 4$.
A comparison of $P^0_{\Omega_{4K}}(\mathbf{w}_k, \boldsymbol{\mathcal{A}}^{PODP-FULL}, \boldsymbol{B}^{DC}_{0,hq}, \boldsymbol{u}^{PODP-FULL})$ with $P^0_{\Omega_{4K}}(\mathbf{w}_k, \boldsymbol{\mathcal{A}}^{AC}_{\varepsilon,hq}, \boldsymbol{B}^{DC}_{0,hq}, \boldsymbol{u}^{AC}_{hp})$ is provided in Figure 19a. Similarly a comparison of $E^k_{\Omega_{4K}}(\mathbf{w}_k, \boldsymbol{u}^{PODP-FULL})$ with $E^k_{\Omega_{4K}}(\mathbf{w}_k, \boldsymbol{u}^{AC}_{hp})$ is shown in Figure 19b. It can be observed that an excellent agreement with the full order solution is obtained. Excellent agreement is also observed in the other shields and we refer to [38] for further details. Note that the result in the 4K shield is shown as it is in this shield where the biggest variations in the dissipated power and kinetic energy are observed. This is due to the variation in shielding effect of the 77K shield with a changing conductivity. Or in other words, when the conductivity of the 77K shield increases its skin depth reduces, thus the AC magnetic field at the 4K shield decreases.

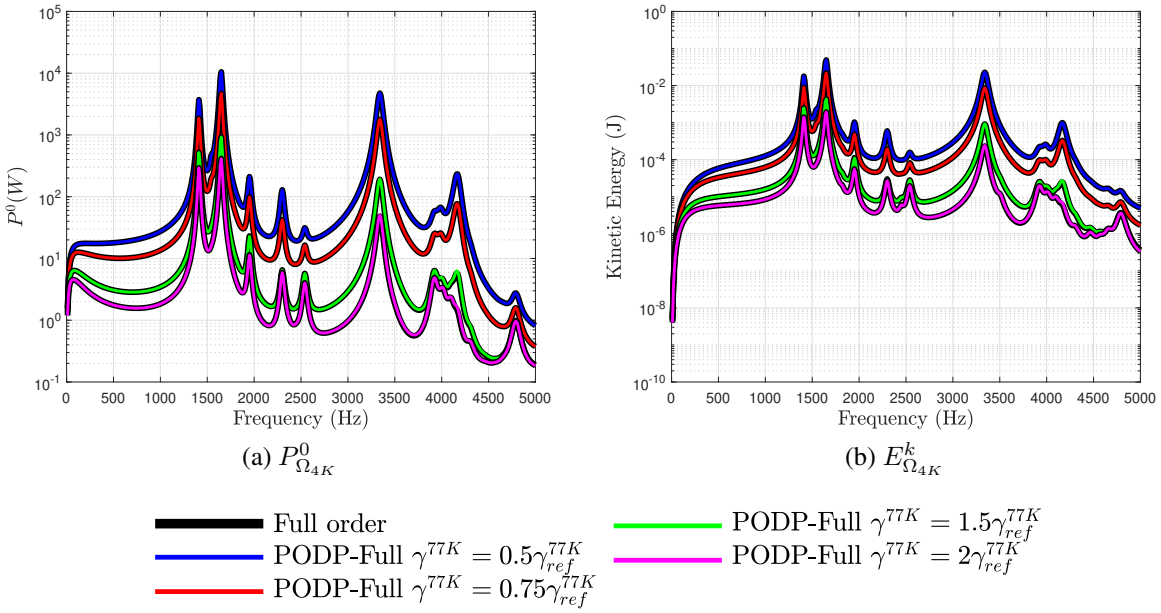

(a) $P^0_{\Omega_{4K}}$ (b) $E^k_{\Omega_{4K}}$

Figure 19: PODP-Full applied to modified magnet problem with multiple parameters: (a) Dissipated power and (b) kinetic energy in Ω_{4K} for different values of γ^{77K}. Comparison with full order solution.

The solver time was again measured and compared with the full order solver in order to study the efficiency of the method. The result is shown in Figure 20, where the total time is shown for the full order case and

the total and off-line times are shown for the PODP-Full case. It can be observed that the speed-up is in this case even higher than for the test magnet problem with z gradient coil and it grows to values above 95 % [10]. This is due to the increased complexity of the electromagnetic problem which results in the need to increase the polynomial order of the $\boldsymbol{H}(\text{curl})$ basis functions to $q = 4$ in order to reach a converged solution. On the other hand, the order of the H^1 basis functions can be kept as $p = 3$ which is the same used for the test magnet problem.

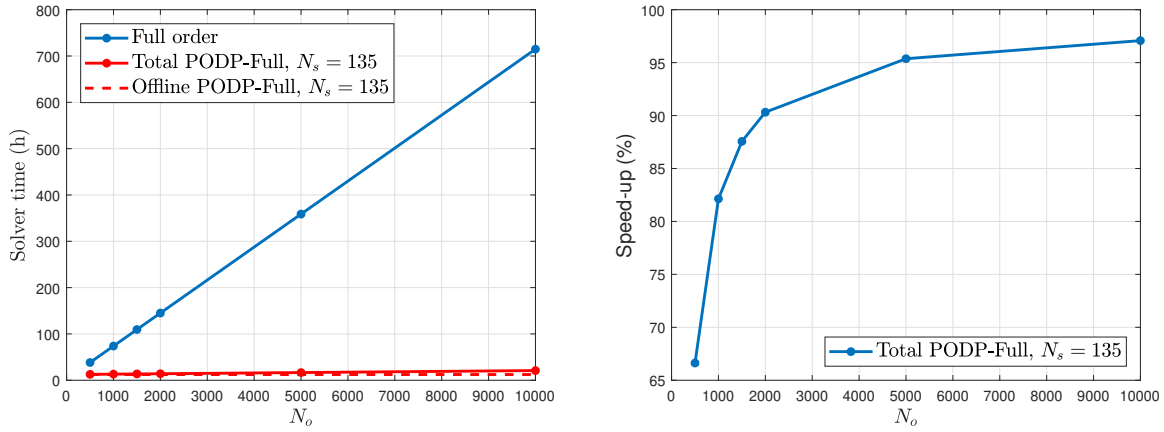

(a) Solver Time

(b) Speed-up

Figure 20: PODP-Full applied to modified magnet problem with multiple parameters: (a) Solver time and (b) speed-up for different values of N_s and N_o.

Next, in order to further assess the accuracy of the method, a contour plot of $|\text{Re}(\boldsymbol{\jmath}^o_{hpq}(\boldsymbol{x}, \mathbf{w}))|$ and $|\text{Re}(\boldsymbol{\jmath}^{PODP-FULL}(\boldsymbol{x}, \mathbf{w}))|$ in the deformed 4K shield for $\mathbf{w} = (8000\pi, 0.5\gamma^{77K}_{ref})$ is presented in Figure 21. It can be observed that an excellent agreement is obtained.
Finally, it is important to remark the capability of the PODP-Full methodology to efficiently conduct on-line multiple queries. To demonstrate this we have computed the response surface for the dissipated power in the radiation shields when varying γ^{77K} and f. The result for $P^0_{\Omega_{4K}}, P^0_{\Omega_{77K}}$ and $P^0_{\Omega_{OVC}}$ is shown in Figure 22. Note that to produce a plot with sufficient resolution we have computed the solution at 8000 sample points, which correspond to the parameters $\mathbf{w}_k = (2\pi \text{f}_i, \gamma^{77K}_j)$, $k = i + (j-1)N_{\omega_o}$, $i = 1, \ldots, N_{\omega_o}$, $j = 1, \ldots, N_{\gamma_o}$, $\text{f}_i = 10 + \Delta\text{f}(i-1)$, $\Delta\text{f} = 10$ Hz, $N_{\omega_o} = 500$, $\gamma^{77K}_j = 0.5\gamma^{77K}_{ref} + \Delta\gamma(j-1)\gamma^{77K}_{ref}$ S/m, $\Delta\gamma = 0.1$ and $N_{\gamma_o} = 16$. Thus, according to Figure 20, the time required to compute this response surface with the full order solver would be almost 600 h, while with PODP-Full methodology it reduces to 20 h (including the off-line stage), with a speed up of 96 %. Note that the on-line stage is even much faster and, thus, the methodology can be used to, once the off-line solution is computed, produce multiple results similar to those shown in Figure 22 in a very efficient manner.

7 Conclusions

The application of POD to 3D coupled magneto-mechanical problems with application to MRI scanners has been studied in this paper. First, we considered the direct application of POD to the coupled physics problem and we showed that the number of snapshots required to obtain an accurate approximation is very large and thus no computational speed-up can be obtained with this method. This is due to the singularities in the mechanical displacements associated with the resonant modes of the mechanical system. Motivated by this, a novel combined reduced order-full order methodology that exploits the staggered nature of the

[10] Note again that for the time of the full order solver only the first 4 points of the curve were measured and the last two were extrapolated.

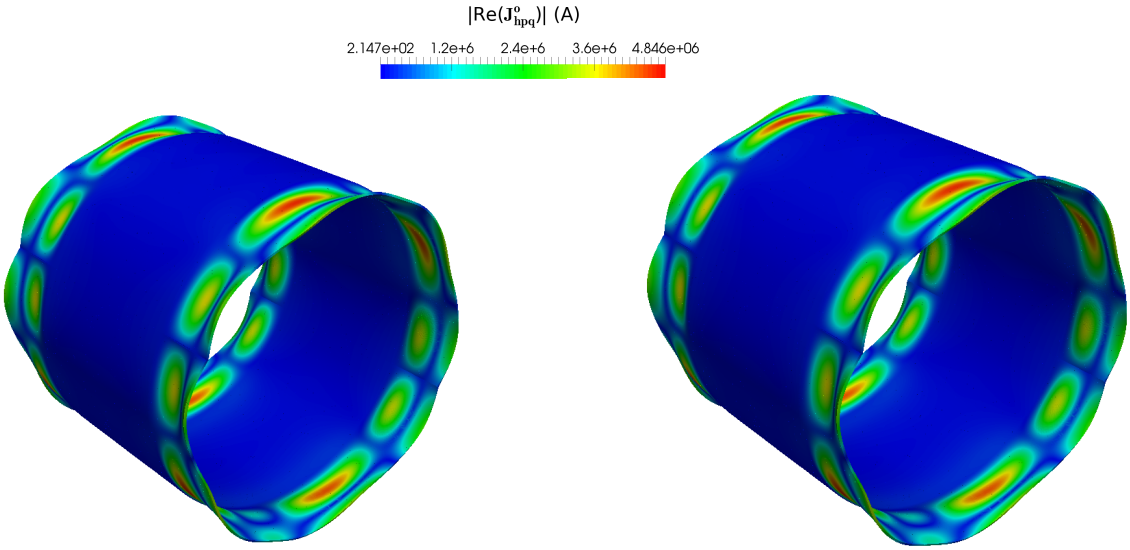

(a) $|\text{Re}(\boldsymbol{\jmath}^o_{hpq}(\boldsymbol{x}, \mathbf{w}))|$ (b) $|\text{Re}(\boldsymbol{\jmath}^{PODP-FULL}(\boldsymbol{x}, \mathbf{w}))|$

Figure 21: PODP-Full applied to modified magnet problem with multiple parameters: Contours of (a) $|\text{Re}(\boldsymbol{\jmath}^o_{hpq}(\boldsymbol{x}, \mathbf{w}))|$ and (b) $|\text{Re}(\boldsymbol{\jmath}^{PODP-FULL}(\boldsymbol{x}, \mathbf{w}))|$ in the deformed 4K shield for $\mathbf{w} = (8000\pi, 0.5\gamma^{77K}_{ref})$. Deformation exaggerated by a factor of 10^4.

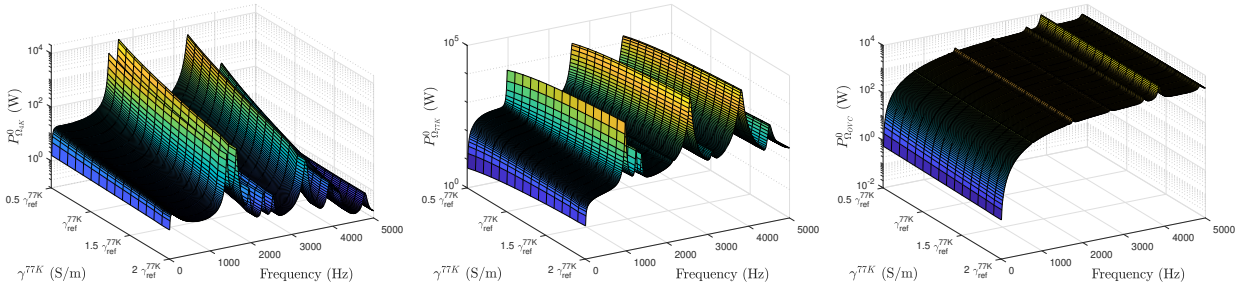

(a) $P^0_{\Omega_{4K}}$ (b) $P^0_{\Omega_{77K}}$ (c) $P^0_{\Omega_{OVC}}$

Figure 22: PODP-Full applied to modified magnet problem with multiple parameters: Response surface for (a) $P^0_{\Omega_{4K}}$, (b) $P^0_{\Omega_{77K}}$ and (c) $P^0_{\Omega_{OVC}}$ for varying γ^{77K} and f.

problem was proposed. This methodology consists in applying POD only to the electromagnetic problem and using this to feed the mechanical full order solver. The accuracy and efficiency of this methodology were proven by applying it to challenging MRI configurations, which showed that PODP gives an increased accuracy compared to PODI for no significant increase in computational cost and that a massive speed-up of up to 97 % is achieved, especially when N_o is large. Hence, the methodology can be applied in order to significantly decrease the design time of new MRI scanners, which has positive implications in terms of cost and competitiveness.

Acknowledgements

The authors would like to thank the European Commission for the funding received through the Marie Sklodowska-Curie Innovative Training Network AdMoRe with grant number 675919.
S.Zlotnik was partially funded by the Spanish Ministry of Economy and Competitiveness (grant number DPI2017-85139-C2-2-R) and by the Generalitat de Catalunya (grant number 2017-SGR-1278).

Appendix

A Affine Decomposition in terms of Frequency and Conductivity

The only matrix block of $\mathbf{A}$ in (15) that depends on frequency and conductivity is $\mathbf{C}^{\mathrm{AC}}_{\mathcal{A}\mathcal{A}}$[11]. Consider the general case of a problem with N_C disjoint conducting subdomains, $\Omega_{C,n}$, $n = 1, 2, \ldots, N_C$ with conductivities $\gamma = \gamma_n$ in $\Omega_{C,n}$. An exact affine decomposition in terms of frequency and conductivity can then be achieved by rewriting $\mathbf{C}^{\mathrm{AC}}_{\mathcal{A}\mathcal{A}}$ as

$$\mathbf{C}^{\mathrm{AC}}_{\mathcal{A}\mathcal{A}} = \mathrm{i}\omega \sum_{n=1}^{N_C} \gamma_n \mathbf{C}^{\mathrm{AC},\Omega_{C,n}}_{\mathcal{A}\mathcal{A}} + \omega\varepsilon \mathbf{C}^{\mathrm{AC},\Omega^e_C}_{\mathcal{A}\mathcal{A}},$$

where we have defined the matrices $\mathbf{C}^{\mathrm{AC},\Omega_{C,n}}_{\mathcal{A}\mathcal{A}}$ and $\mathbf{C}^{\mathrm{AC},\Omega^e_C}_{\mathcal{A}\mathcal{A}}$. Then, the matrix products

$$\tilde{\mathbf{K}}^{\mathrm{AC}}_{\mathcal{A}\mathcal{A}} = \left(\mathbf{H}^M\right)^* \mathbf{K}^{\mathrm{AC}}_{\mathcal{A}\mathcal{A}} \mathbf{H}^M, \tag{33a}$$

$$\tilde{\mathbf{C}}^{\mathrm{AC},\Omega^l_C}_{\mathcal{A}\mathcal{A}} = \left(\mathbf{H}^M\right)^* \mathbf{C}^{\mathrm{AC},\Omega^l_C}_{\mathcal{A}\mathcal{A}} \mathbf{H}^M, \tag{33b}$$

$$\tilde{\mathbf{C}}^{\mathrm{AC},\Omega^e_C}_{\mathcal{A}\mathcal{A}} = \left(\mathbf{H}^M\right)^* \mathbf{C}^{\mathrm{AC},\Omega^e_C}_{\mathcal{A}\mathcal{A}} \mathbf{H}^M, \tag{33c}$$

$$\tilde{\mathbf{K}}^{\mathrm{AC}}_{\mathcal{U}\mathcal{A}} = \left(\mathbf{H}^M\right)^* \mathbf{K}^{\mathrm{AC}}_{\mathcal{U}\mathcal{A}} \mathbf{H}^M, \tag{33d}$$

$$\tilde{\mathbf{K}}^{\mathrm{AC}}_{\mathcal{U}\mathcal{U}} = \left(\mathbf{H}^M\right)^* \mathbf{K}^{\mathrm{AC}}_{\mathcal{U}\mathcal{U}} \mathbf{H}^M, \tag{33e}$$

$$\tilde{\mathbf{C}}^{\mathrm{AC}}_{\mathcal{U}\mathcal{U}} = \left(\mathbf{H}^M\right)^* \mathbf{C}^{\mathrm{AC}}_{\mathcal{U}\mathcal{U}} \mathbf{H}^M, \tag{33f}$$

$$\tilde{\mathbf{M}}^{\mathrm{AC}}_{\mathcal{U}\mathcal{U}} = \left(\mathbf{H}^M\right)^* \mathbf{M}^{\mathrm{AC}}_{\mathcal{U}\mathcal{U}} \mathbf{H}^M, \tag{33g}$$

can be precomputed at the *off-line* stage and the reduced matrix is built in the general case as

$$\mathbf{A}^M = \begin{bmatrix} \tilde{\mathbf{K}}^{\mathrm{AC}}_{\mathcal{A}\mathcal{A}} + \varepsilon\omega \tilde{\mathbf{C}}^{\mathrm{AC},\Omega^e_C}_{\mathcal{A}\mathcal{A}} + \mathrm{i}\omega \sum_{n=1}^{N_C} \gamma_n \tilde{\mathbf{C}}^{\mathrm{AC},\Omega_{C,n}}_{\mathcal{A}\mathcal{A}} & \mathbf{0} \\ \tilde{\mathbf{K}}^{\mathrm{AC}}_{\mathcal{U}\mathcal{A}} & \tilde{\mathbf{K}}^{\mathrm{AC}}_{\mathcal{U}\mathcal{U}} + \mathrm{i}\omega \tilde{\mathbf{C}}^{\mathrm{AC}}_{\mathcal{U}\mathcal{U}} - \omega^2 \tilde{\mathbf{M}}^{\mathrm{AC}}_{\mathcal{U}\mathcal{U}} \end{bmatrix}, \tag{34}$$

where all the costly matrix products have been precomputed and the only operations to be performed at the *on-line* stage are scalar times matrix products and sum of matrices. Furthermore, the affine decomposition can be used to speed-up the *off-line* stage, or the full order solution for varying parameters, as the parameter independent blocks are assembled only once and the system matrix is then constructed as

$$\mathbf{A} = \begin{bmatrix} \mathbf{K}^{\mathrm{AC}}_{\mathcal{A}\mathcal{A}} + \varepsilon\omega \mathbf{C}^{\mathrm{AC},\Omega^e_C}_{\mathcal{A}\mathcal{A}} + \mathrm{i}\omega \sum_{n=1}^{N_C} \gamma_n \mathbf{C}^{\mathrm{AC},\Omega_{C,n}}_{\mathcal{A}\mathcal{A}} & \mathbf{0} \\ \mathbf{K}^{\mathrm{AC}}_{\mathcal{U}\mathcal{A}} & \mathbf{K}^{\mathrm{AC}}_{\mathcal{U}\mathcal{U}} + \mathrm{i}\omega \mathbf{C}^{\mathrm{AC}}_{\mathcal{U}\mathcal{U}} - \omega^2 \mathbf{M}^{\mathrm{AC}}_{\mathcal{U}\mathcal{U}} \end{bmatrix}. \tag{35}$$

Note that for application to the separated physics, as described in Section 5.2, the methodology can be applied analogously by considering only the relevant blocks of the global matrix.

[11] Note that the dependency of the mechanical damping and mass blocks on ω has already been written in an affine format.

References

[1] D. Amsallem and C. Farhat. Interpolation method for adapting reduced-order models and application to aeroelasticity. *AIAA journal*, 46(7):1803–1813, 2008.

[2] S. Bagwell. *A Numerical Multi-Physics Approach to Understanding MRI Scanners and their Complex Behaviour*. PhD thesis, Swansea University, UK., 2018.

[3] S. Bagwell, P. D. Ledger, A. J. Gil, and M. Mallett. Transient solutions to nonlinear acousto-magneto-mechanical coupling for axisymmetric MRI scanner design. *International Journal for Numerical Methods in Engineering*, 115(2):209–237, 2018.

[4] S. Bagwell, P. D. Ledger, A. J. Gil, M. Mallett, and M. Kruip. A linearised hp-finite element framework for acousto- magneto-mechanical coupling in axisymmetric MRI scanners. *International Journal for Numerical Methods in Engineering*, 112:1323–1352, 2017.

[5] R. A. Bialecki, A. J. Kassab, and A. Fic. Proper orthogonal decomposition and modal analysis for acceleration of transient FEM thermal analysis. *International Journal for Numerical Methods in Engineering*, 62(6):774–797, 2005.

[6] A. Bjorck. *Numerical Methods for Least Squares Problems*. SIAM, Philadelphia, USA, 1996.

[7] T. Bui-Thanh, M. Damodaran, and K. Willcox. Proper orthogonal decomposition extensions for parametric applications in compressible aerodynamics. In *21st AIAA Applied Aerodynamics Conference*, DOI:10.2514/6.2003-4213, 2003.

[8] V. Buljak. *Inverse Analyses with Model Reduction: Proper Orthogonal Decomposition in Structural Mechanics*. Springer Science & Business Media, Berlin, Germany, 2011.

[9] A. Chatterjee. An introduction to the proper orthogonal decomposition. *Current Science*, 78(7):808–817, 2000.

[10] F. Chinesta, R. Keunings, and A. Leygue. *The Proper Generalized Decomposition for Advanced Numerical Simulations: A Primer*. Springer Science & Business Media, Berlin, Germany, 2013.

[11] F. Chinesta and P. Ladevèze. *Separated Representations and PGD-Based Model Reduction: Fundamentals and Applications*. International Centre for Mechanical Siences, Courses and Lectures. Springer, Vienna, Austria, 2014.

[12] N. Demo, N. Tezzele, G. Gustin, G. Lavini, and G. Rozza. Shape optimisation by means of proper orthogonal decomposition and dynamic mode decomposition. In *Technology and Science for the Ships of the Future: Proceedings of NAV 2018: 19th International Conference on Ship & Maritime Research*, pages 212–219, 2018.

[13] S. Georgaka, G. Stabile, G. Rozza, and M. J. Bluck. Parametric POD-Galerkin model order reduction for unsteady-state heat transfer problems. *arXiv:1808.05175v3*, 2018.

[14] G. Giovannetti, V. Hartwig, V. Viti, P. Zadaricchio, L. Meini, L. Landini, and A. Benassi. Low field elliptical MR coil array designed by FDTD. *Concepts in Magnetic Resonance Part B: Magnetic Resonance Engineering: An Educational Journal*, 33(1):32–38, 2008.

[15] P. C. Hansen. *Rank-Deficient and Discrete Ill-Posed Problems: Numerical Aspects of Linear Inversion*. SIAM, Philadelphia, USA, 2005.

[16] J. S. Hesthaven, G. Rozza, B. Stamm, et al. *Certified Reduced Basis Methods for Parametrized Partial Differential Equations*. Springer, Cham, Switzerland, 2016.

[17] T. J. R. Hughes. *The Finite Element Method: Linear Static and Dynamic Finite Element Analysis*. Dover Publications, New York, USA, 2012.

[18] D. Kalman. A singularly valuable decomposition: the SVD of a matrix. *The College Mathematics Journal*, 27(1):2–23, 1996.

[19] J. Kerler-Back and T. Stykel. Model reduction for linear and nonlinear magneto-quasistatic equations. *International Journal for Numerical Methods in Engineering*, 111(13):1274–1299, 2017.

[20] D. Lazzaro and L. B. Montefusco. Radial basis functions for the multivariate interpolation of large scattered data sets. *Journal of Computational and Applied Mathematics*, 140(1-2):521–536, 2002.

[21] P. D. Ledger. hp-Finite element discretisation of the electrical impedance tomography problem. *Computer Methods in Applied Mechanics and Engineering*, 225:154–176, 2012.

[22] P. D. Ledger, A. J. Gil, R. Poya, M. Kruip, I. Wilkinson, and S. Bagwell. Solution of an industrially relevant coupled magneto-mechanical problem set on an axisymmetric domain. *Applied Mathematical Modelling*, 40:1959–1971, 2016.

[23] P. D. Ledger and S. Zaglmayr. hp-Finite element simulation of three-dimensional eddy current problems on multiply connected domains. *Computer Methods in Applied Mechanics and Engineering*, 199:3386–3401, 2010.

[24] X. Liang, J. Zhang, M. Zhang, and L. Cui. Multivariate Lagrange interpolation and an application of Cayley-Bacharach theorem for it. *arXiv:math/0608115v2*, 2006.

[25] Y. C. Liang, H. P. Lee, S. P. Lim, W. Z. Lin, K. H. Lee, and C. G. Wu. Proper orthogonal decomposition and its applications—Part I: Theory. *Journal of Sound and Vibration*, 252(3):527–544, 2002.

[26] F. Liu and S. Crozier. An FDTD model for calculation of gradient-induced eddy currents in MRI system. *IEEE Transactions on Applied Superconductivity*, 14(3):1983–1989, 2004.

[27] Z. Luo, J. Du, Z. Xie, and Y. Guo. A reduced stabilized mixed finite element formulation based on proper orthogonal decomposition for the non-stationary Navier–Stokes equations. *International Journal for Numerical Methods in Engineering*, 88(1):31–46, 2011.

[28] D. Modesto, S. Zlotnik, and A. Huerta. Proper generalized decomposition for parameterized Helmholtz problems in heterogeneous and unbounded domains: Application to harbor agitation. *Computer Methods in Applied Mechanics and Engineering*, 295:127–149, 2015.

[29] S. Niroomandi, I. Alfaro, E. Cueto, and F. Chinesta. Model order reduction for hyperelastic materials. *International Journal for Numerical Methods in Engineering*, 81(9):1180–1206, 2010.

[30] M. Oulghelou and C. Allery. Non intrusive method for parametric model order reduction using a bi-calibrated interpolation on the Grassmann manifold. *arXiv preprint arXiv:1901.03177*, 2018.

[31] C. L. Pettit and P. S. Beran. Application of proper orthogonal decomposition to the discrete Euler equations. *International Journal for Numerical Methods in Engineering*, 55(4):479–497, 2002.

[32] A. Radermacher and S. Reese. POD-based model reduction with empirical interpolation applied to nonlinear elasticity. *International Journal for Numerical Methods in Engineering*, 107(6):477–495, 2016.

[33] R. R. Rama. *Proper Orthogonal Decomposition with Interpolation-Based Real-Time Modelling of the Heart*. PhD thesis, University of Cape Town, South Africa, 2017.

[34] R. R. Rama, S. Skatulla, and C. Sansour. Real-time modelling of the heart using the proper orthogonal decomposition with interpolation. In *VI International Conference on Computational Bioengineering ICCB*, pages 1–12, Barcelona, Spain, 2015.

[35] M. Rausch, M. Gebhardt, M. Kaltenbacher, and H. Landes. Computer-aided design of clinical magnetic resonance imaging scanners by coupled magnetomechanical-acoustic modeling. *IEEE Transactions on Magnetics*, 41:72–81, 2005.

[36] G. Rozza, H. Malik, N. Demo, M. Tezzele, M. Girfoglio, G. Stabile, and A. Mola. Advances in reduced order methods for parametric industrial problems in computational fluid dynamics. *arXiv preprint arXiv:1811.08319*, 2018.

[37] J. Schöberl and S. Zaglmayr. High order Nédélec elements with local complete sequence properties. *The International Journal for Computation and Mathematics in Electrical and Electronic Engineering (COMPEL)*, 24:374–384, 2005.

[38] M. Seoane. *3D Simulation of Magneto-Mechanical Coupling in MRI Scanners Using High Order FEM and POD*. PhD thesis, Swansea University, UK., 2019.

[39] M. Seoane, P. D. Ledger, A. J. Gil, and M. Mallet. An accurate and efficient three dimensional high order finite element methodology for the simulation of magneto-mechanical coupling in MRI scanners. *International Journal for Numerical Methods in Engineering*, 119(12):1185–1215, 2019.

[40] G. Stabile, S. Hijazi, A. Mola, S. Lorenzi, and G. Rozza. POD-Galerkin reduced order methods for CFD using Finite Volume Discretisation: vortex shedding around a circular cylinder. *Communications in Applied and Industrial Mathematics*, 8(1):210–236, 2017.

[41] E. Süli and D. Mayers. *An Introduction to Numerical Analysis*. Cambridge University Press, Cambridge, UK., 2003.

[42] A. Trakic, H. Wang, F. Liu, H. Lopez, and S. Crozier. Analysis of transient eddy currents in MRI using a cylindrical FDTD method. *IEEE Transactions on Applied Superconductivity*, 16(3):1924–1936, 2006.

[43] F. Vetrano, C. Le Garrec, G. D. Mortchelewicz, and R. Ohayon. Assessment of strategies for interpolating POD based reduced order models and application to aeroelasticity. *Journal of Aeroelasticity and Structural Dynamics*, 2(2), 2012.

[44] Y. Wang, B. Yu, Z. Cao, W. Zou, and G. Yu. A comparative study of POD interpolation and POD projection methods for fast and accurate prediction of heat transfer problems. *International Journal of Heat and Mass Transfer*, 55(17-18):4827–4836, 2012.